Quantum optics with nitrogen-vacancy centers in diamond

Yiwen Chu and Mikhail D. Lukin

Department of Physics, Harvard University, Cambridge, MA 02138 USA

Contents

1

Quantum optics with nitrogen-vacancy centers in diamond

1.1 Background

The study of classical mechanics, thermodynamics, and electromagnetism have brought on great technological advances over the course of history. We now live in an exciting era where quantum mechanics begins to join these other fields of physics in enabling new technologies with unprecedented capabilities. Theoretical and experimental efforts have moved toward harnessing the power of various different physical systems for applications in metrology, quantum information, and furthering our understanding of quantum mechanics itself.

Some of the most successful of applications of quantum mechanical systems to date have been in the field of metrology, or the accurate sensing and measurement of forces, fields, frequencies, etc. (Chou *et al.*, 2010; Nicholson *et al.*, 2012; Benko *et al.*, 2012; Kessler *et al.*, 2012). At the same time, the field of quantum information and communications has become the focus of much effort in recent years. There has been a large number of theoretical proposals for using quantum systems for efficient computation, simulation of complex systems, secure dissemination of information, etc. (Shor, 1994; Kimble, 2008; Lloyd, 1996). However, the practical implementation of these proposals in real physical systems remains an open challenge. A variety of different avenues are being actively explored, ranging from photons, neutral atoms, ions, impurities and structures in solid state systems, to more exotic materials such as electrons on the surface of liquid helium (Monroe and Kim, 2013; Awschalom *et al.*, 2013; Clarke and Wilhelm, 2008; Stern and Lindner, 2013; Platzman and Dykman, 1999). A common theme for the implementation of quantum technologies involves addressing the seemingly contradictory need for controllability and isolation from external effects. Undesirable effects of the environment must be minimized, while at the same time techniques and tools must be developed that enable us to interact with the system in a controllable and well-defined manner. These lectures address several aspects of this theme with regards to a particularly promising candidate for developing applications in both metrology and quantum information: the nitrogen-vacancy (NV) center in diamond. In particular, we explore how the NV center can be investigated, controlled, and efficiently coupled with optical photons, and tackle the challenges of controlling the optical properties of these emitters inside a complex solid-state environment. Some recent reviews on NV centers can be found in (Jelezko and Wrachtrup, 2006; Doherty *et al.*, 2013; Doherty *et al.*, 2012).

As with other solid state systems such as quantum dots, rare earth dopants in inorganic crystals, and superconducting qubits, NV centers present the attractive feature of eliminating the need for trapping and cooling, as is usually required for atomic systems. In addition to greatly reducing the complexity of experiments, solid state systems offer the possibility of straightforward integration with fabricated structures and development of scalable quantum devices. The issue of scalability, however, is not simply a matter of being able to create a large number of physical devices in a small volume. In order to truly move beyond proof-of-principle experiments, the properties of many qubits and devices must all be well controlled in a reproducible, reliable, and efficient manner. In other words, while it is important to demonstrate that a certain quantum operation, coherence time, metrological sensitivity, etc. is possible in one particular device with favorable characteristics, it must also be possible to reproduce these characteristics for a large number of systems.

Diamond is a particularly promising host material for optically active quantum emitters due to its wide bandgap (5.5 eV) and large transparency window. It supports a huge variety of impurities and defects that give rise to optical bands at energies throughout the infrared and visible spectrum (Zaitsev, 2010). The NV center is unique in that it combines well-defined optical transitions with long-lived spin sub-levels in the ground state, much like alkali atoms with transitions involving hyperfine sublevels. The present lectures focus on quantum optical experiments with NV centers. In recent years, a comprehensive theoretical model has been developed to describe the spin and optical properties of the NV center, which has been reviewed in (Maze *et al.*, 2011; Doherty *et al.*, 2012; Doherty *et al.*, 2010). We begin by summarizing this theoretical framework, which allows us to understand the underlying physics of the subsequent experimental results. We then describe the experimental techniques that are used to investigate and address the optical properties of NV centers. As part of this description, we will encounter some general characteristics of the system that will be come important issues to be addressed later, such as the Debye-Waller factor and the sensitivity of the excited state to the local environment. Based on our theoretical understanding and spectroscopic results, we show that NV centers offer a rich set of possibilities for experiments demonstrating coherent optical control of the system, several of which are summarized in the remainder of the chapter.

1.2   Level structure and polarization properties of the NV center

As is the case in any system, the electronic structure of the NV center can be analyzed by considering its symmetry, in addition to the various interactions that are present. Our description below starts with electronic states that obey the C_{3v} symmetry of the NV center. We then consider the effect of various interactions one by one, starting from the the Coulomb interaction, which sets the energy scale of the optical transitions. Spin-orbit and spin-spin interactions act to lift the degeneracy of the different states in the ground and excited state manifolds. Finally, we consider the effect of external perturbations such as electric and magnetic fields that change the nature and energies of the unperturbed states. More detailed analysis of many of the concepts presented in this section can be found in (Maze *et al.*, 2011).
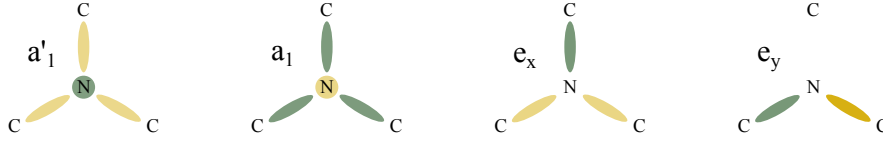
Fig. 1.1 Single electron orbitals of the NV center. The nitrogen and three carbons surrounding the vacancy are shown, and the perspective is along the NV axis. The color scale roughly represents the sign and occupation of each orbital.

1.2.1 Electronic states of the NV center

The negatively-charged NV center has six electrons, five of which are from the nitrogen and the three carbons surrounding the vacancy. They occupy the orbitals states a'_1, a_1, e_x, e_y, which are combinations of the four dangling bonds surrounding the vacancy that satisfy the symmetry imposed by the nuclear potential. They can be written as

$$a'_1 = \alpha \frac{\sigma_1 + \sigma_2 + \sigma_3}{3} + \beta \sigma_n, \tag{1.1}$$

$$a_1 = \beta \frac{\sigma_1 + \sigma_2 + \sigma_3}{3} + \alpha \sigma_n, \tag{1.2}$$

$$e_x = \frac{2\sigma_1 - \sigma_2 - \sigma_3}{\sqrt{6}}, \tag{1.3}$$

$$e_y = \frac{\sigma_2 - \sigma_3}{\sqrt{2}} \tag{1.4}$$

where σ_1, σ_2, σ_3 and σ_n are the dangling bonds from the three carbons and the nitrogen, respectively. These orbitals transform as the irreducible representations of the C_{3v} group and have been extensively used by many authors (Loubser and Wyk, 1978; Goss *et al.*, 1996; Lenef and Rand, 1996; Gali *et al.*, 2008). They are schematically illustrated in Figure 1.1 to give an idea of their symmetries. From these pictorial representations, one can deduce that, for example, $\langle e_y | \hat{y} \cdot \vec{r} | e_x \rangle = \langle e_x | \hat{x} \cdot \vec{r} | e_x \rangle = -\langle e_y | \hat{x} \cdot \vec{r} | e_y \rangle \neq 0$. This means that the $|e_x\rangle$ and $|e_y\rangle$ states have permanent electric dipole moments, which will become important later for understanding the electric field sensitivity of the NV center's excited states and spectral diffusion of the optical transitions. In addition, one also sees that $\langle a | \hat{x} \cdot \vec{r} | e_x \rangle = \langle a | \hat{y} \cdot \vec{r} | e_y \rangle \neq 0$, which gives rise to the transition dipole moments between the ground and excited states. These properties will be discussed in more detail in the following sections.

In the ground state of the NV center, the a'_1 and a_1 states, which are lowest in energy, are filled by four electrons, as shown in Figure 1.2. The remaining two electrons occupy the degenerate orbitals e_x and e_y. The orbitals e_x and e_y can be viewed as p-type orbitals and $e_+ = -e_x - ie_y$, $e_- = e_x - ie_y$ are analogous to p states with definite orbital angular momentum. An antisymmetric combination of the orbital states minimizes the Coulomb energy and results in a spin-triplet ground state manifold
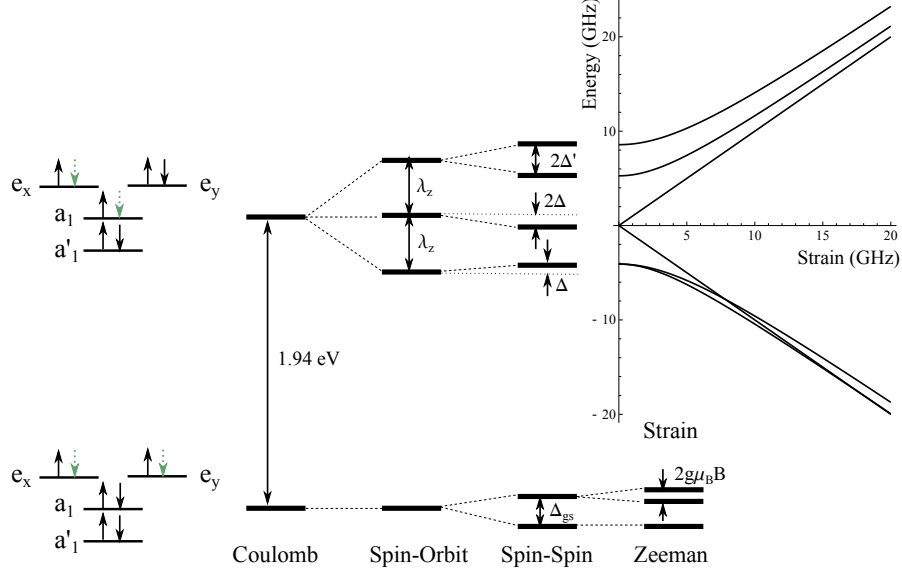
Fig. 1.2 Ground and excited states associated with the NV center's optical transitions. The four symmetrized states are filled by six electrons, which can also be viewed as two holes (indicated with green arrows). The Coulomb interaction defines the optical transition energy of the NV center. The effect of the spin-orbit and spin-spin interactions are indicated for both the ground and excited states. In the ground state, the application of a magnetic field further splits the $|m_s = \pm 1\rangle$ states due to the Zeeman interaction. In the excited state, crystal strain modifies the energies of sublevels. See (Maze et al., 2011) for details.

$$\left|{}^3 A_2\right\rangle = |E_0\rangle \otimes \begin{cases} |+1\rangle \\ |0\rangle \\ |-1\rangle \end{cases} \tag{1.5}$$

where $|\pm 1\rangle, |0\rangle$ correspond to the $m_s = \pm 1, 0$ states, respectively. The notation $|E_0\rangle = |e_x e_y - e_y e_x\rangle$ indicates that the orbital state has 0 orbital angular momentum projection along the NV axis. A_2 denotes the orbital symmetry of the state, which is determined by the symmetries of the e_x and e_y orbitals. From here on, we will often denote these ground states simply as $|0\rangle$ and $|\pm 1\rangle$ when it's clear that we are referring to the full electronic state and not just the spin projections.

The relevant excited state for the optical transitions of the NV center is a pair of triplets which arises from the promotion of one of the electrons occupying the orbital a_1 to the e_x or e_y orbitals (Goss *et al.*, 1996). Note that this state can be modeled by one hole in the orbital e and another hole in the orbital a_1, i.e. a triplet in the ae electronic configuration (similarly, the ground state can be modeled by two holes in the e^2 electronic configuration). A total of six states can be formed in this configuration and their symmetries are determined by a group theoretical analysis (Maze *et al.*, 2011),

$$|A_1\rangle = |E_-\rangle \otimes |+1\rangle - |E_+\rangle \otimes |-1\rangle$$

$$|A_2\rangle = |E_-\rangle \otimes |+1\rangle + |E_+\rangle \otimes |-1\rangle$$
$$|E_x\rangle = |X\rangle \otimes |0\rangle$$
$$|E_y\rangle = |Y\rangle \otimes |0\rangle \qquad\qquad (1.6)$$
$$|E_1\rangle = |E_-\rangle \otimes |-1\rangle - |E_+\rangle \otimes |+1\rangle$$
$$|E_2\rangle = |E_-\rangle \otimes |-1\rangle + |E_+\rangle \otimes |+1\rangle$$

where we have named the first four states as A_1, A_2, E_x and E_y according to their symmetries and named the last two states as E_1 and E_2 since they also transform according to the irreducible representation E. Here, $|E_\pm\rangle = |ae_\pm - e_\pm a\rangle$ and $|X(Y)\rangle = |ae_{x(y)} - e_{x(y)}a\rangle$.

As spin-orbit and spin-spin interactions are invariant under any operation of the C_{3v} group, the states given in equation (1.6) are eigenstates of the full Hamiltonian including these interactions and in the absence of any perturbation such as magnetic field and/or crystal strain. The Hamiltonians for the spin-orbit and spin-spin interactions can be written in the basis of the six states listed above as

$$H_{so} = \lambda_z \left(|A_1\rangle\langle A_1| + |A_2\rangle\langle A_2| - |E_1\rangle\langle E_1| - |E_2\rangle\langle E_2| \right) \qquad (1.7)$$
$$H_{ss} = \Delta \left(|A_1\rangle\langle A_1| + |A_2\rangle\langle A_2| + |E_1\rangle\langle E_1| + |E_2\rangle\langle E_2| \right)$$
$$-2\Delta \left(|E_x\rangle\langle E_x| + |E_y\rangle\langle E_y| \right) + \Delta' \left(|A_2\rangle\langle A_2| - |A_1\rangle\langle A_1| \right)$$
$$+\Delta'' \left(|E_1\rangle\langle E_y| + |E_y\rangle\langle E_1| - i|E_2\rangle\langle E_x| + i|E_x\rangle\langle E_2| \right) \qquad (1.8)$$

where λ_z is the axial spin-orbit interaction and $3\Delta \approx 1.42$ GHz and $\Delta' \approx 1.55$ GHz characterize the spin-spin induced zero-field splittings (Lenef and Rand, 1996; Rogers *et al.*, 2009; Maze *et al.*, 2011). It can be seen that spin-orbit interaction splits states with different total angular momentum, i.e., the pairs (A_1, A_2), (E_x, E_y) and (E_1, E_2) are split from each other by about 5.5 GHz (Lenef and Rand, 1996; Manson *et al.*, 2006; Batalov *et al.*, 2009). The Δ'' term leads to non-spin preserving cross transitions, which results to optical pumping of the spin states and plays a role in, for example, limiting the efficiency of spin readout using resonant excitation. The spin-spin interaction also plays a crucial role in the stability of the states $|A_1\rangle$ and $|A_2\rangle$. This interaction shifts up the non-zero spin states (A_1, A_2, E_1 and E_2) by $\sim \frac{1}{3}1.42$ GHz (Fuchs *et al.*, 2008; Batalov *et al.*, 2009) and shift the states $|E_x\rangle$ and $|E_y\rangle$ down by $\sim \frac{2}{3}1.42$ GHz. Thus, the gap between (A_1, A_2) and (E_x, E_y) is increased, but the gap between the states (E_x, E_y) and (E_1, E_2) is reduced. In addition, the spin-spin interaction splits the states $|A_2\rangle$ and $|A_1\rangle$ by ~ 3.3 GHz (Batalov *et al.*, 2009). Thus, for relatively low strain, we obtain a very robust $|A_2\rangle$ state with stable symmetry properties that are protected by an energy gap arising from the spin-orbit and spin-spin interactions.

We note here that the zero-field splitting in the ground state also arises from the spin-spin interaction, and gives an energy difference of $\Delta_{gs} \sim 2.88$ GHz between the $|m_s = 0\rangle$ and $|m_s = \pm 1\rangle$ states.

1.2.2 Properties of optical transitions

Once the wavefunctions are known, it is possible to calculate the selection rules of optical transitions between the triplet excited state and the triplet ground state. The

Table 1.1 Selection rules for optical transitions between the triplet excited state (ae) and the triplet ground state (e^2). Linear polarizations are represented by $\hat{x}$ and $\hat{y}$, while circular polarization are represented by $\hat{\sigma}_\pm = \hat{x} \pm i\hat{y}$. As an example, a photon with σ_+ polarization is emitted when the electron decays from state A_2 to state ${}^3A_{2-}$.

Pol	A_1	A_2	E_1	E_2	E_x	E_y
${}^3A_{2-}$	$\hat{\sigma}_+$	$\hat{\sigma}_+$	$\hat{\sigma}_-$	$\hat{\sigma}_-$		
${}^3A_{20}$					$\hat{y}$	$\hat{x}$
${}^3A_{2+}$	$\hat{\sigma}_-$	$\hat{\sigma}_-$	$\hat{\sigma}_+$	$\hat{\sigma}_+$		

dipole moment between the ground and excited state is produced by the hole left in the a orbital under optical excitation. As mentioned earlier, the matrix elements $\langle a| \hat{x} \cdot \vec{r} |e_x\rangle$ and $\langle a| \hat{y} \cdot \vec{r} |e_y\rangle$ are non-zero, where $\hat{x}$ and $\hat{y}$ represent the polarization of the involved photon. We can then calculate the selection rules for transitions between every pair of ground and excited states, as shown in Table 1.1. As expected, these selection rules conserve the total angular momentum of the photon-NV center system.

The allowed optical transitions and their polarization properties indicate several possible Λ schemes in the NV center. However, while these properties are relatively robust in the $|A_1\rangle$ and $|A_2\rangle$ states, the $|A_1\rangle$ state is coupled non-radiatively to a metastable singlet state, which then decays to the ground state $|0\rangle$. This results in leakage out of the Λ system consisting of the $|A_1\rangle$ state and the $|\pm 1\rangle$ states. Thus, we find that the $|A_2\rangle$ state provides the an almost ideal closed Λ scheme for experiments such as spin-photon entanglement, as described in Section 1.6 and (Togan *et al.*, 2010). On the other hand, the open Λ system involving $|A_1\rangle$ can be useful for efficient detection of dark states during coherent population trapping, as shown in Section 1.7 and (Togan *et al.*, 2011).

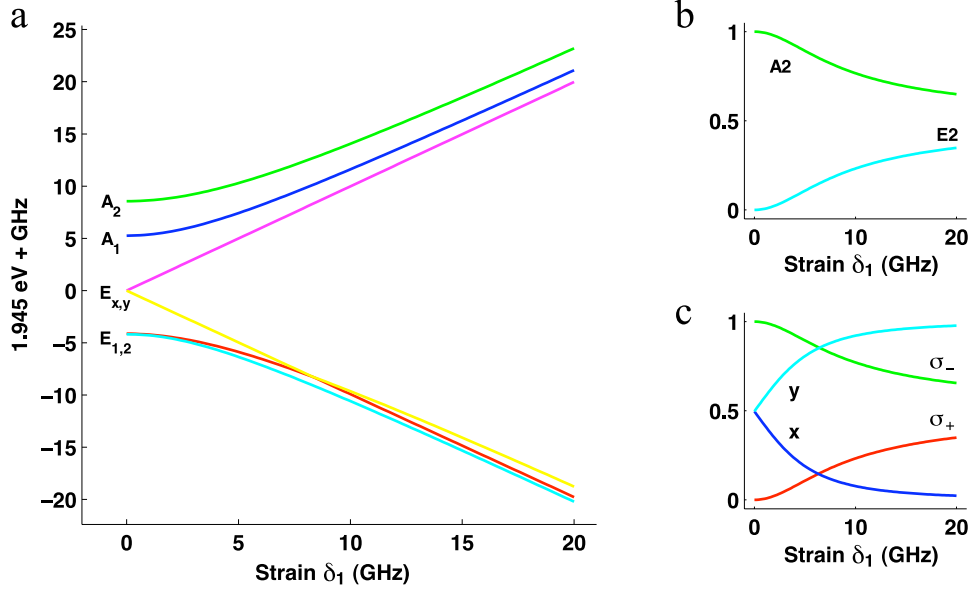### 1.2.3 The effect of strain

We now discuss the effect of local strain on the properties of the optical transitions in order to understand variations between different NV centers and deviations from the unperturbed system described above. This perturbation splits the degeneracy between the e_x and e_y orbitals and results in their mixing. In the limit of high strain (larger than the spin-orbit splitting), the excited state manifold splits into two triplets, each with a particular well defined spatial wavefunction. Orbital and spin degrees of freedom separate in this regime and spin-preserving transitions are excited by linearly polarized light. The strain Hamiltonian is given by (Rogers *et al.*, 2009; Maze *et al.*, 2011)

$$H_{strain} = \delta_1 \left(|e_x\rangle\langle e_x| - |e_y\rangle\langle e_y| \right) + \delta_2 \left(|e_x\rangle\langle e_y| + |e_y\rangle\langle e_x| \right) \tag{1.9}$$

where δ_1 and δ_2 are different parameters describing the crystal strain. Figure 1.3 shows an example of how δ_1 strain splits and mixes the excited states, and as a results changes the polarization properties of the optical transitions. A similar effect occurs for δ_2 strain, where $|A_2\rangle$ is mixed with $|E_1\rangle$.

The full Hamiltonian for the excited state manifold of the NV center is then

$$H = H_{ss} + H_{so} + H_{strain}, \tag{1.10}$$

Fig. 1.3 Effect of strain on the properties of the NV center. **a.** Energies of the excited states as a function of strain, expressed in units of the linear strain induced splitting between the $|E_x\rangle$ and $|E_y\rangle$ states. **b.** Strain induced mixing of the $|A_2\rangle$ and $|E_2\rangle$ states, showing the fraction of A_2 and E_2 character of the highest energy excited state. **c.** Polarization character of the optical transition between $|A_2\rangle$ state and the ground state $|+1\rangle$ as a function of strain. As strain increases, the polarization changes from circularly to linearly polarized. The transition between $|A_2\rangle$ and $|-1\rangle$ shows the same behavior, except with σ_- and σ_+ switched. Therefore, at high strain, decay from the $|A_2\rangle$ results in a separable state of the photon polarization and spin rather than an entangled state.

which can be written in the set of basis states $\{|A_1\rangle, |A_2\rangle, |E_x\rangle, |E_y\rangle, |E_1\rangle, |E_2\rangle\}$ as

$$
H = \begin{pmatrix}
\Delta - \Delta' + \lambda_z & 0 & 0 & 0 & \delta_1 & -i\delta_2 \\
0 & \Delta + \Delta' + \lambda_z & 0 & 0 & i\delta_2 & -\delta_1 \\
0 & 0 & -2\Delta + \delta_1 & \delta_2 & 0 & i\Delta'' \\
0 & 0 & \delta_2 & -2\Delta - \delta_1 & \Delta'' & 0 \\
\delta_1 & -i\delta_2 & 0 & \Delta'' & \Delta - \lambda_z & 0 \\
i\delta_2 & -\delta_1 & -i\Delta'' & 0 & 0 & \Delta - \lambda_z
\end{pmatrix}
\tag{1.11}
$$

It is worth mentioning that while the excited state configuration is highly affected by strain, the ground state configuration is unaffected to first order due to its anti-symmetric combination of e_x and e_y orbitals. It is also protected by the large optical gap between the ground and excited state to second order perturbation in strain.

1.3   Experimental techniques

Having developed a theoretical model for the optical transitions of the NV center, we now move on to experimental explorations of these properties. While there are many

available descriptions of setups and procedures for room temperature experiments with NV centers (Gruber *et al.*, 1997; Childress *et al.*, 2006), we will focus here on some techniques relevant for low-temperature studies of the optical properties.

1.3.1   Diamond materials

We begin this section with a description of different types of single crystal diamond samples and their properties with regard to NV center properties. The first type of commonly available diamond material is classified as type Ib. In these diamonds, substitutional nitrogen atoms (also called P1 centers) are the dominant defects, which cause the samples to have a yellow color (Zaitsev, 2010). Type Ib diamonds can occur naturally and are typically grown by the high-pressure-high-temperature (HPHT) method by companies such as Element Six and Sumitomo. Element Six specifies their type Ib diamond as having substitutional nitrogen concentrations of <200 ppm. In our experience, the concentration of NV centers in type Ib samples vary widely through different samples, but NV centers in bulk samples are usually unresolvable under confocal microscopy. There have been no reports of coherent optical transitions from type Ib diamonds, except in one nanocrystal sample where a narrow, but spectrally unstable line was observed under photoluminescence excitation (PLE) spectroscopy (Shen *et al.*, 2008). However, as far as we know, this result has never been reproduced. In our experiments, type Ib samples are typically used for developing and fabricating nanophotonic structures and studies of NV centers in these structures at room temperature.

The rest of the diamond samples that are suitable for the experiments described here can be classified as type IIa, which is typically defined as having nitrogen impurity concentrations of less than 1ppm. Type IIa diamonds are rare in nature, but one such sample was found containing a resolvable concentration of single NV centers that show optical linewidths that are close to the lifetime limited linewidth of 13 MHz (Tamarat *et al.*, 2006). Many initial experiments on the optical properties of NV centers were performed on several different pieces of this sample, including the ones described in Sections 1.6 and 1.7 of this chapter, along with, for example, (Tamarat *et al.*, 2006) and (Batalov *et al.*, 2008). The unique properties of this sample, and its somewhat exotic origins in the Ural mountains, has earned it the nickname "The Magic Russian Diamond". The piece used in our experiments is shown in Figure 1.4a. Clearly, such specialized samples cannot be used for wide-scale experiments and development of diamond-based devices. An alternative is to work with synthetic type IIa diamonds grown using microwave assisted chemical vapor deposition (CVD) at companies such as Element Six Inc. Standard type IIa grade samples typically also show a unresolvable concentration of NV centers. However, "electronic grade" diamonds developed by Element Six, which are specified to have substitutional nitrogen concentrations of <5 ppb, have NV center concentrations that range from barely resolvable single NVs to less than 1 NV per tens of μm^3. Native NV centers found in these samples often have linewidths that are broadened by spectral diffusion to several hundred MHz (Bernien *et al.*, 2012; Acosta *et al.*, 2012; Stacey *et al.*, 2012). However, they have been used in a variety of experiments involving optical transitions of NV centers (Bernien *et al.*, 2013; Bernien *et al.*, 2012; Sipahigil *et al.*, 2012), and are also excellent starting materials
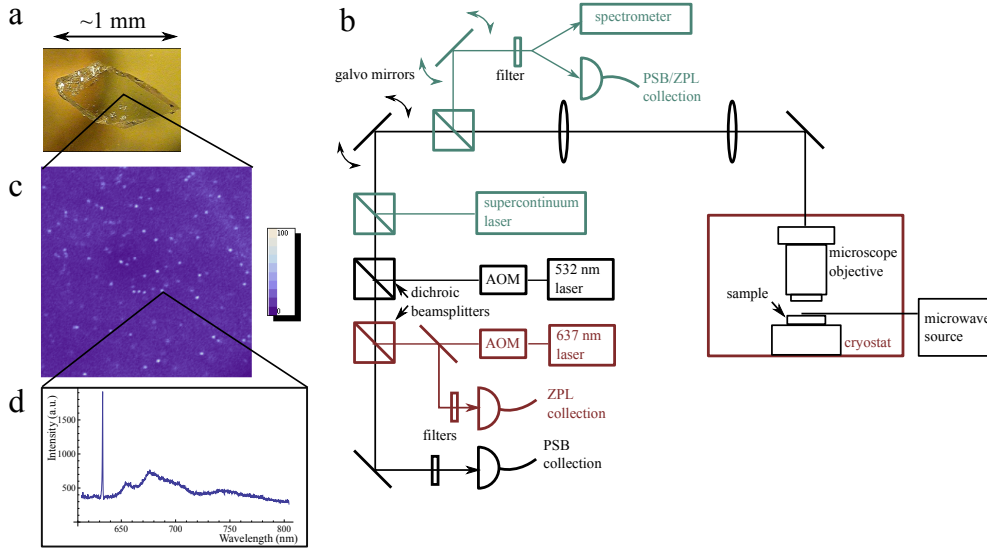
Fig. 1.4 Experimental setup and characterization of NV centers. **a.** The type IIa natural diamond sample used for the experiments in Sections 1.6 and 1.7. **b.** Confocal microscope setup. Components in black are needed for a basic room temperature apparatus for investigating the ground state spin physics of the NV center. Red components, such as a cryostat and resonant excitation laser, are additionally needed for low temperature studies of coherent optical properties. A supercontinuum laser is added for characterization of photonic devices such as cavities and waveguides, and an additional, independent collection channel is used for collecting light from a different spatial location than the excitation, as shown in green. In addition, the spectrometer can also be used for photoluminescence studies for the NV center. **c.** Confocal image of single NV centers obtained using 532 nm excitation and PSB collection. **d.** Low temperature photoluminescence spectrum of a NV center. Sharp peak is ZPL at 637 nm.

for introducing optically coherent NV centers through ion implantation, as described in Section 1.8.

1.3.2 Experimental setup for optical characterization of NV centers

Figure 1.4b shows a schematic of a multi-purpose setup used for optical investigation of NV centers and diamond-based photonic devices. Depending on the type of experiment, only parts of this comprehensive setup are needed. A typical basic confocal microscope for room-temperature studies of NV centers is shown in black. A high numerical aperture (NA) objective is used to focus laser light onto the sample. In order to scan over the sample and locate individual centers in a confocal image such as shown in Figure 1.4c, the diamond is either mounted on a high resolution positioning stage, or the optical path is scanned using a galvo mirror imaged onto the back of the objective with a pair of lenses comprising a 4f imaging system. The vibronic sidebands of the NV center's optically excited states can be addressed using a laser of higher energy than the 637 nm zero-phonon line (ZPL). Typically, this is

done using a 532 nm frequency doubled Nd:YAG laser, which is the most common method for controlling the charge state of the NV center. CW 532 nm excitation can ionize both the negatively charged NV center and surrounding charge donors such as substitutional nitrogens, resulting in a equilibrium charge state of the NV center that is $\sim 70\%$ NV$^-$ and $\sim 30\%$ NV^0 (Aslam *et al.*, 2013). Off resonant excitation is also used in room temperature experiments to polarize the spin of the NV center in to the $|m_s = 0\rangle$ ground state. This process happens through non-spin preserving transitions from the optically excited state into spin-singlet states of the NV center, which then preferentially decays to the $|m_s = 0\rangle$ state (Manson *et al.*, 2006). Finally, microwave and RF fields for driving spin transitions of the NV centers can be applied with a variety of methods, including copper wires, coplanar waveguides, and resonator structures.

For low temperature experiments, the diamond sample is placed inside a helium flow cryostat (Janis ST-500) and cooled to $\sim$4K. Alternative low temperature systems such as closed-cycle pulse tube coolers and bath cryostats can also used. Diamond samples are typically mounted onto the cold finger, or some intermediate substrate such as a silicon wafer, using indium or silver paste. For resonant excitation of the NV centers, a external cavity diode laser around 637 nm is introduced into the optical path. The New Focus TLB 6304 laser is a popular choice due to its large mode-hop-free scanning range of 60-80 GHz, wavelength tunability over several nanometers, and ease of operation. Both the 532 nm and 637 nm lasers need to be pulsed for most experiments, which can be accomplished using acoustic-optical modulators (AOM) or electro-optical modulators (EOM).

Fluorescence from the NV center is collected through the same optical path, coupled into single-mode fibers, and detected using avalanche photodiodes (APD) or a spectrometer. Filters are placed in the collection path to remove reflected excitation light and separate different parts of the emission spectrum. As shown in Figure 1.4d, the NV center spectrum consists of a broad separate phonon-sideband (PSB) and a sharp ZPL at low temperatures. The percentage of emission into the ZPL is typically $3 - 5\%$, which is a major limitation on the efficiency of applications based on coherent photons from the NV center. In Section 1.9, we will address this issue by enhancing the emission into the ZPL using cavity QED with nanophotonic structures. In order to characterize these structures, we use an additional supercontinuum laser as a broadband light source to perform transmission measurements of cavities and waveguides. The light is coupled into one port of the optical device, and the transmitted light must be collected from an output port at a spatially separate location. For this purpose, a second collection channel can be added with its own set of galvo mirrors. In addition, the signal from the two channels can be combined on a time-correlated single photon counting (TCSPC) device for measurements of the second-order autocorrelation function $g^2(\tau)$ of the emission from individual NV centers to show that they are single-photon emitters (Kurtsiefer *et al.*, 2000). This can also be accomplished by splitting the light collected in a single channel using a fiber beamsplitter.

1.4   PLE spectroscopy of NV centers

The optical transitions of the NV center can be identified using PLE spectroscopy by scanning the resonant excitation laser across the ZPL and collecting photons in the PSB. Since the $|0\rangle \rightarrow |E_x\rangle$ and $|0\rangle \rightarrow |E_y\rangle$ are best the cycling transitions, they are usually the ones observed in PLE spectroscopy in the absence of microwave driving or laser modulation. However, repeated resonant excitation eventually ionizes the NV^- and optically pumps the NV center into a different ground state spin sublevel due to the small non-spin conserving cross transitions out of the $|m_s = 0\rangle$ excited states into the $|\pm 1\rangle$ ground states (Tamarat *et al.*, 2008). Therefore, some form of charge and spin repumping must eventually be performed. As shown in Figure 1.5b, the first method we use involves scanning the 637 nm laser across the NV transitions and turning on the laser while simultaneous collecting PSB counts for $\sim$ 2 ms at each frequency. At the end of the scan, the 637 nm laser is turned off and a 532 nm repumping pulse is applied. Any duration of repumping longer than a few μs is sufficient to reinitialize the NV center. Depending on the charge environment of the NV center and its strain-dependent level structure, however, it may be difficult to obtain good signal from this simple method. For example, in the presence of a large number of other charge traps in the environment, the NV center may be ionized before a sufficient number of photons are scattered on resonance. Another potential issue is that the $|0\rangle \rightarrow |E_x\rangle$ and $|0\rangle \rightarrow |E_y\rangle$ transitions have some branching ratio into the $m_s = \pm 1$ states, causing a decrease in fluorescence on the timescale of several microseconds. However, fluorescence can potentially still be detected due to off-resonant excitation of transitions from the $|\pm 1\rangle$ spin states. For example, at high strain, the $|\pm 1\rangle \rightarrow |A_1\rangle$ transition becomes almost degenerate with the $|\pm 1\rangle \rightarrow |E_x\rangle$ transition, allowing a steady state fluorescence to be established. However, this may not be the case for all NV centers. More robust methods of obtaining the PLE spectrum without repumping during the scan involve either CW microwave mixing of the $|0\rangle$ and $|\pm 1\rangle$, or modulation of the resonant excitation laser by the ground state zero-field splitting, which also allows the $|m_s = \pm 1\rangle$ transitions to be observed (Tamarat *et al.*, 2008; Fu *et al.*, 2009; Santori *et al.*, 2006).

Figure 1.5b shows the results of PLE scans taken using this first method. A clear resonance can be seen in each scan, whose frequency then jumps during each successive scan. This is an indication of spectral diffusion, where changes in the local electric field environment of the NV center causes the energies of its excited states to fluctuate over time. As mentioned earlier, from the electronic orbitals $|e_x\rangle$ and $|e_y\rangle$ involved in the excited states, one can see that the $|E_x\rangle$ and $|E_y\rangle$ states have a permanent electric dipole moment. This dipole moment has been measured to be $\sim$0.8 Debye, which gives rise to energy shifts of $\sim$4 GHz/MV/m (Maze *et al.*, 2011). It is now well established that 532 nm repumping causes complex charge dynamics in the diamond environment by photoionizing impurities that act as charge donors (Bassett *et al.*, 2011). Therefore, while very narrow single-scan linewidths can be obtained using this method (Shen *et al.*, 2008; Tamarat *et al.*, 2006; Fu *et al.*, 2009), the long-term, extrinsically broadened linewidth obtained by averaging many such scans can be much broader (Bernien *et al.*, 2012; Acosta *et al.*, 2012; Stacey *et al.*, 2012). This issue is addressed in more detail in Section 1.8 of this chapter.
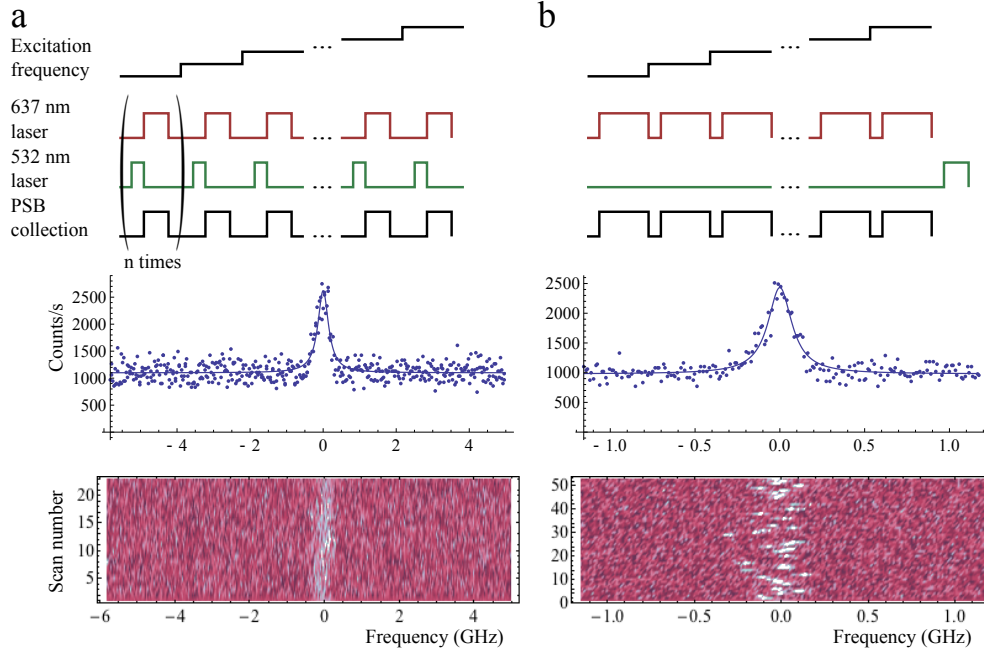
Fig. 1.5 Methods for PLE spectroscopy of NV centers. **a.** Pulse sequence for repumping during each PLE scan (top), along with an example showing the result of successive scans (bottom) and the averaged spectrum (middle). **b.** Pulse sequence for repumping at the end of each PLE scan (top), along with corresponding results for the same transition as in a., except zoomed in over a smaller frequency range.

A second method of obtaining the PLE spectrum involves a pulse sequence consisting of a 1 μs 532 nm repumping pulse, followed by a 10 μs resonant excitation pulse, during which PSB counts are collected. As the 637 nm laser is scanned across the NV transitions, this sequence is repeated many times for each frequency, as illustrated in Figure 1.5. This method has the advantage that it is robust against ionization and spin polarization, and should in principle give good signal to noise regardless of the charge environment and strain-dependent level structure of the NV center. It also shows the overall lineshape of the transition, including effects of spectral diffusion, in a single scan. Again, microwave fields are used to obtain a spectrum of all the possible transitions, including those that involve the $|m_s = \pm 1\rangle$ states.

1.5 Optical properties of NV centers

Figure 1.6a shows a PLE spectrum taken with CW microwave excitation that mixes the ground states during the 637 nm laser pulse. All resonances expected from the direct and cross transitions are observed, as shown in 1.6b, along with some possible microwave-optical two photon transitions.

The strongest transitions in 1.6a are the $|0\rangle \rightarrow |E_x\rangle$ and $|0\rangle \rightarrow |E_y\rangle$ cycling transitions. Figure 1.7a shows an example of optical Rabi oscillations on the $|0\rangle \rightarrow |E_y\rangle$
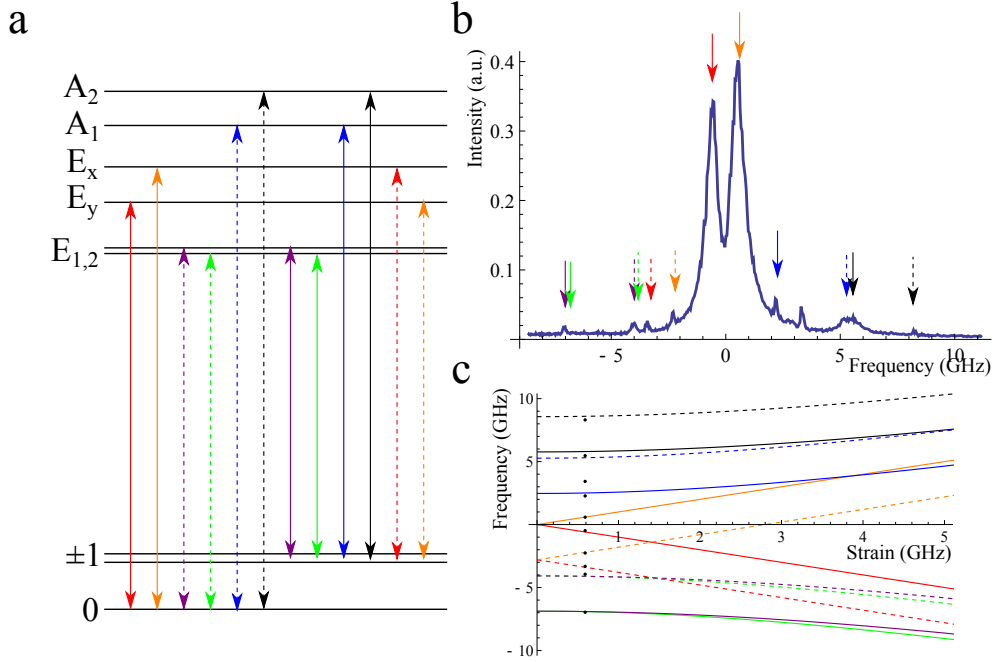
Fig. 1.6 Optical transitions of the NV center. **a.** All possible transitions between the ground and excited states, with direct transitions indicated with solid lines, and spin non-conserving cross transitions indicated with dashed lines. **b.** PLE spectrum taken with CW microwave excitation. **c.** Frequencies of all possible transitions shown in a. as a function of strain. The frequencies of the peaks in b. are matched to a particular strain value. The extra unidentified peak may be due to a two photon transition from the $|0\rangle$ state to the $|E_x\rangle$ state through the absorption of an optical photon and emission of a microwave photon.

transition, measured by turning on a 40 ns resonant laser pulse a rise time of ~ 1 ns using an EOM (Guided Color Technologies). We then accumulate a histogram of photon arrival times on a TCSPC device with a timing resolution of 195 ps. The photon count rate is proportional to the population in the $|E_y\rangle$ state, which, in the absence of decay or decoherence, is given by $P_{E_y}(t) = \cos^2(|\Omega|t)$, where $\Omega = \vec{\mu} \cdot \vec{E}/\hbar$ is the Rabi frequency. In this case, however, the oscillations are damped by the finite lifetime of the excited states, which can be measured by fitting to the exponentially decaying tail after the pulse turns off. In addition to population decay, additional decoherence, such as frequency fluctuations of the transition frequency relative to the laser frequency caused by, for example, spectral diffusion, will also contribute to the damping of Rabi oscillations. We note here, however, that this additional dephasing alone does not always give a good estimate of the spectral diffusion of the NV center, unlike what is sometimes claimed in literature. For example, if the transition frequency jumps well outside of the power-broadened linewidth of the transition, then the NV center will effectively not be excited, and there will simply be no contribution to the Rabi oscillation data.
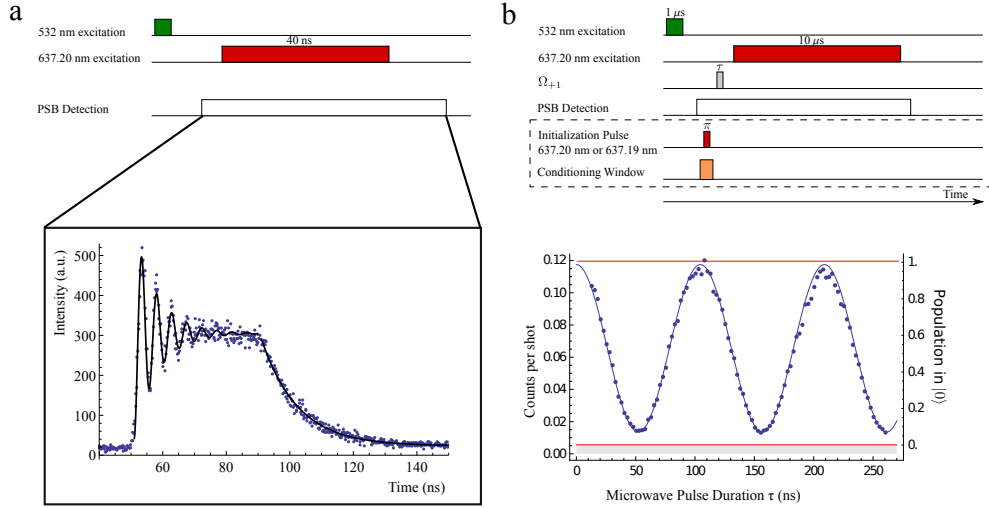
Fig. 1.7 a. Optical Rabi oscillations detected using PSB fluorescence and resonant excitation, along with corresponding pulse sequence. The 637.2 nm laser is tuned to the $|0\rangle \rightarrow |E_y\rangle$ transition and is on from 50 ns to 90 ns. **b.** Rabi oscillations between $|0\rangle$ and $|+1\rangle$ (blue) detected using resonant spin readout and corresponding pulse sequence. Red lines are calibration levels for the $|0\rangle$ and $|+1\rangle$ states. To initialize the spin states for this calibration, we use a measurement-based technique where the $|0\rangle$ is prepared conditioned on the detection of a PSB photon after excitation to the $|E_y\rangle$ state. To prepare the $|+1\rangle$ state, we then apply a microwave π pulse before readout.

By measuring Rabi oscillations, we can determine the length of laser pulse needed to, for example, perform an optical π pulse to transfer population to the $|A_2\rangle$ state for entanglement generation, as described in Section 1.6. Note that, while optical Rabi oscillations can also be observed between the $|m_s = \pm 1\rangle$ ground and excited states, the dynamics are more complicated due to the fact that these are Λ-type transitions. In the absence of a magnetic field, instead of settling to a steady state value corresponding to 50% population in the excited state, the photon count rate continually decreases after a few optical cycles as population is pumped into a "dark" ground state that is not excited by the by the laser. However, the observed Rabi oscillations are usually sufficient for determining the optical π pulse length.

The cycling transitions of the NV center can also be used to efficiently read out the spin state of the NV center. As shown in Figure 1.7, when a resonant laser pulse is turned on for 10 μs, the number of photons scattered is proportional to the population in the $|m_s = 0\rangle$ states, and microwave-driven Rabi oscillations between the $|0\rangle$ and $|+1\rangle$ ground state sublevels can be observed. A detailed description of the resonant spin-readout procedure used in Section 1.6 can be found in (Togan *et al.*, 2010). The efficiency and fidelity of this spin readout method is limited by the photon collection efficiency, the temperature, and the branching ratio out of the $|m_s = 0\rangle$ manifold. As can be predicted by the Hamiltonian given in Equation 1.2.3, this branching ratio depends on the local strain. In our first experiments, the spin readout contrast was

limited to $c_M = 0.11 \pm 0.0022$ counts/shot when the spin was prepared in the $|0\rangle$ state and a background-limited $c_B = 0.0057 \pm 0.0010$ counts/shot when the spin was prepared in the $|\pm1\rangle$ states. Therefore, to determine the spin of the NV center, the state had to be prepared and read-out many times to obtain an average number of counts per shot C, which then allows us to calculate the population in the $|0\rangle$ state as $P = (C - c_B) / (c_M - c_B)$. By increasing the collection efficiency with a solid immersion lens and working with low strain NV centers, single shot resonant readout of the spin state has subsequently been demonstrated (Robledo *et al.*, 2011).

The rest of the chapter gives several examples of applications based on the optical properties of NV centers that we have just described.

1.6 Quantum entanglement between an optical photon and a solid-state spin qubit

1.6.1 Introduction

A quantum network (Kimble, 2008) consists of several nodes, each containing a long-lived quantum memory and a small quantum processor, that are connected via entanglement. Its potential applications include long-distance quantum communication and distributed quantum computation (Duan and Monroe, 2008). Several recent experiments demonstrated on-chip entanglement of solid-state qubits separated by nanometer (Neumann *et al.*, 2008) to millimeter (Ansmann *et al.*, 2009; DiCarlo *et al.*, 2009) length scales. However, realization of long-distance entanglement based on solid-state systems coupled to single optical photons (de Riedmatten *et al.*, 2008) is an outstanding challenge. The NV center is a promising candidate for implementing a quantum node. The ground state of the negatively charged NV center is an electronic spin triplet with a 2.88 GHz zero-field splitting between the $|m_s = 0\rangle$ and $|m_s = \pm1\rangle$ states (from here on denoted $|0\rangle$ and $|\pm1\rangle$). With long coherence times (Balasubramanian *et al.*, 2009), fast microwave manipulation, and optical preparation and detection (Fuchs *et al.*, 2009), the NV electronic spin presents a promising qubit candidate. Moreover, it can be coupled to nearby nuclear spins that provide exceptional quantum memories and allows for the robust implementation of few-qubit quantum registers (Neumann *et al.*, 2008; Dutt *et al.*, 2007). In this section we demonstrate the preparation of quantum entangled states between a single photon and the electronic spin of a NV center:

$$|\Psi\rangle = \frac{1}{\sqrt{2}}(|\sigma_-\rangle\,|+1\rangle + |\sigma_+\rangle\,|-1\rangle), \tag{1.12}$$

where $|\sigma_+\rangle$ and $|\sigma_-\rangle$ are orthogonal circularly polarized single photon states.

The scheme we use here is inspired by previous work done in trapped ions (Blinov *et al.*, 2004). The key idea of our experiment is illustrated in Figure 1.8. The NV center is prepared in a specific excited state ($|A_2\rangle$ in Fig 1.8) that decays with equal probability into two different long lived spin states ($|\pm1\rangle$) by the emission of orthogonally polarized optical photons at 637 nm. The entangled state given by Eq. 1.12 is created because photon polarization is uniquely correlated with the final spin state. This entanglement is verified by spin state measurement using a cycling optical transition following the detection of a 637 nm photon of chosen polarization.
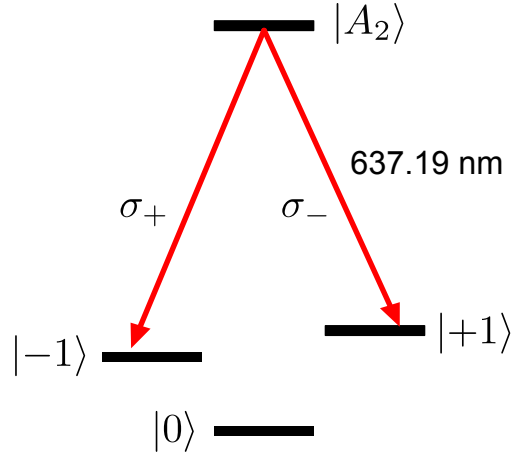
Fig. 1.8 Scheme for spin-photon entanglement. Following selective excitation to the $|A_2\rangle$ state, the Λ system decays to two different spin states through the emission of orthogonally polarized photons, resulting in spin-photon entanglement.

1.6.2 Experimental demonstration of spin-photon entanglement

We now turn to the experimental demonstration of spin-photon entanglement. The experimental setup is outlined in (Togan *et al.*, 2010). To create the entangled state, we use coherent emission within the narrow-band zero phonon line (ZPL), which includes only 4% of the NV center's total emission. The remaining optical radiation occurs in the frequency shifted phonon side band (PSB), which is accompanied by phonon emission that deteriorates the spin-photon entanglement (Kaiser *et al.*, 2009). Isolating the weak ZPL emission presents a significant experimental challenge due to strong reflections of the resonant excitation pulse reaching the detector. By exciting the NV center with a circularly polarized 2 ns π pulse that is shorter than the emission timescale, we can use detection timing to separate reflection from fluorescence photons. A combination of confocal rejection, modulators, and finite transmittivity of our optics suppresses the reflections sufficiently to clearly detect the NV center's ZPL emission in a 20 ns region.

For photon state determination, ZPL photons in either the $|\sigma_\pm\rangle$ or $|H\rangle = \frac{1}{\sqrt{2}}(|\sigma_+\rangle +$ $|\sigma_-\rangle)$, $|V\rangle = \frac{1}{\sqrt{2}}(|\sigma_+\rangle - |\sigma_-\rangle)$ basis are selected by a polarization analysis stage and detected after an optical path of ~ 2 m. Spin readout then occurs after a 0.5 μs spin memory interval following photon detection by transferring population from either the $|\pm 1\rangle$ states or from their appropriately chosen superposition into the $|0\rangle$ state using microwave pulses $\Omega_{\pm 1}$. The pulses selectively address the $|0\rangle \leftrightarrow |\pm 1\rangle$ transitions with resonant frequencies $\omega_\pm$ that differ by $\delta\omega = \omega_+ - \omega_- = 122$ MHz due to an applied magnetic field. For superpositions of $|\pm 1\rangle$ states an echo sequence is applied before the state transfer to extend the spin coherence time. The transfer is followed by resonant excitation of the $|0\rangle \leftrightarrow |E_y\rangle$ transition and collection of the PSB fluorescence. We carefully calibrate the transferred population measured in the $|0\rangle$ state using the procedure detailed in (Togan *et al.*, 2010). Figure 1.9a shows the populations in the

$|\pm 1\rangle$ states, measured conditionally on the detection of a single circularly polarized ZPL photon. Excellent correlations between the photon polarization and NV spin states are observed.
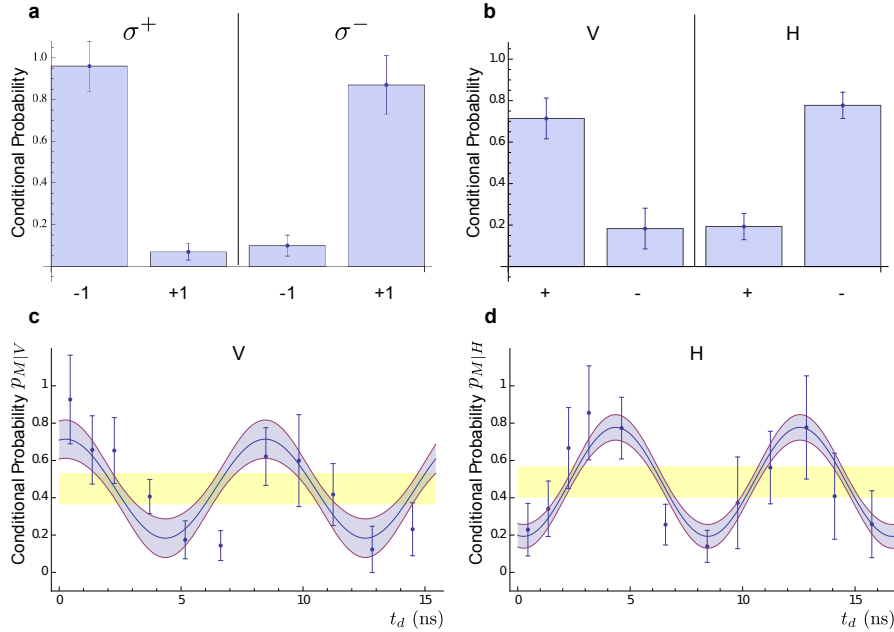
Fig. 1.9 Measurement of spin-photon correlations in two bases. **a.** Conditional probability of measuring $|\pm 1\rangle$ after the detection of a $\sigma+$ or $\sigma-$ photon. **b.** Conditional probability of measuring $|\pm\rangle$ after the detection of a H or V photon, extracted from a fit to data shown in (c) and (d). **c&d.** Measured conditional probability of finding the electronic spin in the state $|M\rangle$ after detection of a V (c) or H (d) photon at time t_d. Blue shaded region is the 68% confidence interval for the fit (solid line) to the time-binned data. Errors on data points are one STD. Combined with the data shown in Figure 1.9(a), oscillations with amplitude outside of the yellow regions result in fidelities greater than 0.5. The visibility of the measured oscillations are 0.59 ± 0.18 (c) and 0.60 ± 0.11 (d). Reprinted from (Togan *et al.*, 2010).

To complete the verification of entanglement, we now show that correlations persist when ZPL photons are detected in a rotated polarization basis. Upon detection of a linearly polarized $|H\rangle$ or $|V\rangle$ photon at time t_d, the entangled state in Eq.1.12 is projected to $|\pm\rangle = \frac{1}{\sqrt{2}} (|+1\rangle \pm |-1\rangle)$, respectively. These states subsequently evolve in time (t) according to

$$|\pm\rangle_t = \frac{1}{\sqrt{2}} \left(e^{-i\omega_+(t-t_d)} |+1\rangle \pm e^{-i\omega_-(t-t_d)} |-1\rangle \right). \tag{1.13}$$

In order to read out the relative phase of superposition states between $|+1\rangle$ and $|-1\rangle$, we use two resonant microwave fields with frequencies ω_+ and ω_- to coherently transfer

the state $|M\rangle = \frac{1}{\sqrt{2}}\left(e^{-i\omega_+ t}\,|+1\rangle + e^{-i(\omega_- t - (\phi_+ - \phi_-))}\,|-1\rangle\right)$ to $|0\rangle$, where the initial relative phase $\phi_+ - \phi_-$ is set to the same value for each round of the experiment. Thus, the conditional probability of measuring the state $|M\rangle$ is

$$p_{M|H,V}\,(t_d) = \frac{1 \pm \cos\alpha\,(t_d)}{2}, \qquad\qquad (1.14)$$

where $\alpha\,(t_d) = (\omega_+ - \omega_-)\,t_d + (\phi_+ - \phi_-)$. Eq. 1.14 indicates that the two conditional probabilities should oscillate with a π phase difference as a function of the photon detection time t_d. This can be understood as follows. In the presence of Zeeman splitting ($\delta\omega \neq 0$) the NV center's spin state is entangled with both the polarization and frequency of the emitted photon. The photon's frequency provides which-path information about its decay. In the spirit of quantum eraser techniques, the detection of $|H\rangle$ or $|V\rangle$ at t_d with high time resolution (~ 300 ps $\ll 1/\delta\omega$) erases the frequency information (Scully and Druhl, 1982; Wilk *et al.*, 2007). When the initial relative phase between the microwave fields $\Omega_{\pm 1}$ is kept constant, the acquired phase difference $(\omega_+ - \omega_-)t_d$ gives rise to oscillations in the conditional probability and produces an effect equivalent to varying the relative phase in the measured superposition, allowing us to verify the coherence of the spin-photon entangled state.

The detection times of ZPL photons are recorded during the experiment without any time gating, which allows us to study spin-photon correlations without reducing the count rate. The resulting data are analyzed in two different ways. First, we time-bin the data and use it to evaluate the conditional probabilities of measuring spin state $|M\rangle$ as a function of $|H\rangle$ or $|V\rangle$ photon detection time (Figures1.9 c,d). Off-diagonal elements of the spin-photon density matrix are evaluated from a simultaneous fit to the binned data and the time bins are chosen to minimize fit uncertainty as described in (Togan *et al.*, 2010). The resulting conditional probabilities are used to evaluate a lower bound on the entanglement fidelity of $F \geq 0.69 \pm 0.068$, above the classical limit of 0.5, indicating the preparation of an entangled state.

We further reinforce our analysis using the method of maximum likelihood estimate. As described in (Togan *et al.*, 2010), this method is applied to raw, un-binned ZPL photon detection and spin measurement data and yields a probability distribution of a lower bound on the fidelity. Consistent with the time-binned approach, we find that our data are described by a near Gaussian probability distribution associated with a fidelity of $F \geq 0.70 \pm 0.070$. Significantly, the cumulative probability distribution directly shows that the measured lower bound on the fidelity is above the classical limit with a probability of 99.7 %.

Several experimental imperfections reduce the observed entanglement fidelity. First, the measured strain and magnetic field slightly mixes $|A_2\rangle$ state with the other excited states. We estimate that $|A_2\rangle$ state imperfection and photon depolarization in the setup together reduce the fidelity by 12 %, the latter being the dominant effect. Imperfections in readout and echo microwave pulses decrease the fidelity by 3 %. Other error sources include finite signal to noise in the ZPL channel (fidelity decrease 11 %), as well as timing jitter (another 4 %). The resulting expected fidelity (73 %) is consistent with our experimental observations. Finally, the entanglement generation

succeeds with probability $p \sim 10^{-6}$, which is limited by low collection and detection efficiency as well as the small probability of ZPL emission.

The demonstration of spin-photon entanglement is the first step in implementing a quantum network architecture for long-distance quantum communications using NV centers (Kimble, 2008). Such an entangled state connects the solid state, spin-based local quantum register with optical photons, which can then be disseminated over free space or through optical fibers. Following the above experiment, tremendous progress has been made in achieving the next steps in building a diamond-based quantum network. Hong-Ou-Mandel interference was demonstrated with indistinguishable photons from remote NV centers hosted in separate diamond samples (Sipahigil *et al.*, 2012; Bernien *et al.*, 2012). Combined with spin-photon entanglement, this recently allowed for the remote entanglement of two NV centers separated by a distance of three meters through entanglement swapping (Bernien *et al.*, 2013).

1.7   Laser cooling and real-time measurement of nuclear spin environment of a solid-state qubit

In this section, we describe the use of the NV center's optical transitions and coherent population trapping (CPT) to sense and manipulate its surrounding spin bath, which consists of the spin of the ^{14}N nucleus associated with the NV center itself and the ^{13}C nuclei in the diamond lattice. Over the past two decades, CPT has been employed for laser cooling of neutral atoms and ions (Aspect *et al.*, 1988), creation of ultra-cold molecules (Ni *et al.*, 2008), optical magnetometry (Scully and Fleischhauer, 1992; Budker and Romalis, 2007), and atomic clocks (Vanier, 2005), as well as for slowing and stopping light pulses (Fleischhauer *et al.*, 2005). The electronic spin of the NV center is a promising system for extending these techniques to the solid state. The NV center has a long-lived spin triplet as its electronic ground state (Manson *et al.*, 2006), whose $m_s = \pm 1, 0$ sublevels are denoted as $|\pm 1\rangle$ and $|0\rangle$. In pure samples, the electron spin dynamics are governed by interactions with the spin-1 ^{14}N nucleus of the NV center and spin–1/2 ^{13}C nuclei present in 1.1 % natural abundance in the diamond lattice (Fig. 1.10a). Control over nuclear spins (Dutt *et al.*, 2007; Neumann *et al.*, 2010) is of interest for both fundamental studies and for applications such as nanoscale magnetic sensing (Maze *et al.*, 2008; Balasubramanian *et al.*, 2008) and realization of quantum networks (Childress *et al.*, 2006; Togan *et al.*, 2010). Here we achieve such control via two complimentary methods: effective cooling of nuclear spins through nuclear state selective CPT (Issler *et al.*, 2010) and conditional preparation based on fast measurements of the nuclear environment and subsequent post-selection (Giedke *et al.*, 2006).

While most prior work involved the use of microwave and RF fields for manipulating both the electronic and nuclear spin states, we utilize all-optical control of the electronic spin (Robledo *et al.*, 2010; Santori *et al.*, 2006; Buckley *et al.*, 2010). Specifically, we make use of Λ-type level configurations involving the NV center's $|A_1\rangle$ and $|A_2\rangle$ optically excited electronic states and the $|\pm 1\rangle$ ground states (Fig. 1.10a) (Togan *et al.*, 2010; Maze *et al.*, 2011). At low temperatures (<10 K) and in the limit of zero strain, $|A_1\rangle$ and $|A_2\rangle$ are entangled states of spin and orbital momentum coupled to the $|+1\rangle$ $(|-1\rangle)$ state with σ_- $(\sigma+)$ circularly polarized light. Correspondingly, excitation

with linearly polarized light drives the NV center into a so-called dark superposition state when the two-photon detuning is zero (Scully and Zubairy, 1997). In the present case the two-photon detuning is determined by the Zeeman splitting between the $|\pm1\rangle$ states due to the combined effect of the Overhauser field originating from the nuclear spin environment and any externally applied magnetic field (Issler *et al.*, 2010; Stepanenko *et al.*, 2006). When the external field exactly compensates the Overhauser field, the electronic spin of the NV center is pumped into the dark state after a few optical cycles and remains in the dark state, resulting in vanishing fluorescence. This is the essence of the dark resonances and CPT.

1.7.1 Coherent population trapping with NV centers

In our experiments, the $|A_1\rangle$ and $|A_2\rangle$ states are separated by approximately 3 GHz and are addressed individually with a single linearly polarized laser at near zero magnetic field. Since there is a finite branching ratio from the $m_s = \pm1$ manifold of the electron spin into the $|0\rangle$ state, we use a recycling laser that drives the transition between $|0\rangle$ and the $|E_y\rangle$ excited state, which decays with a small but non-vanishing probability ($\sim 10^{-2}$) back to the $|\pm1\rangle$ states. Figure 1.10b presents experimental observation of the CPT spectrum as a function of an external magnetic field at three different powers of a laser tuned to the $|\pm1\rangle \rightarrow |A_2\rangle$ transition. While a broad resonance is observed at high power levels, as the power is reduced, we clearly resolve three features in the spectrum separated by 4.4 MHz, which is two times the hyperfine splitting between three ^{14}N nuclear spin states. This separation corresponds to the magnetic field required to bring the electronic $m_s = \pm1$ hyperfine states with equal nuclear spin projection ($m_I = \pm1, 0$) into two-photon resonance.

The dependance of the CPT resonance width upon the laser power, shown in Figure 1.10c, reveals an important role played by repumping on the near-cycling $|0\rangle \leftrightarrow |E_y\rangle$ transition. In contrast to a conventional, closed three-level system, this recycling transition can be used to enhance the utility of our CPT system by both decreasing the width of the CPT resonance and increasing the signal to noise ratio. The $|A_1\rangle$ state decays into the $m_s = 0$ ground state through the singlet with a substantial probability of $\sim 40\%$. However, the population is returned back into the $m_s = \pm1$ state from $|E_y\rangle$ only after ~ 100 optical excitation cycles. As a result, away from the two-photon resonance, the NV quickly decays to the $|0\rangle$ state after being excited, where it then scatters many photons through the $|0\rangle \leftrightarrow |E_y\rangle$ cycling transition before returning to the Λ system. If the NV center is not in a dark state, this process effectively increases the number of photons we collect by $2/\eta = \gamma_{s1}/\gamma_{ce}$, where γ_{ce} is the cross transition rate from $|E_y\rangle$ into $|\pm1\rangle$ and γ_{s1} is the rate from $|A_1\rangle$ to the singlet. The cycling effect also reduces the width of the CPT line since the $|0\rangle \leftrightarrow |E_y\rangle$ transition is quickly saturated away from two-photon resonance, provided that the CPT laser excitation rate exceeds the leakage rate out of recycling transition. Significantly, both of these effects lead to improved sensitivity of dark resonances to small changes in two-photon detuning.

To demonstrate this effect, the widths of dark resonances observed via excitation of $|A_1\rangle$ and $|A_2\rangle$ are compared in Figure 1.10c. Through an independent measurement of the branching ratios (see (Togan *et al.*, 2011)), we determined that
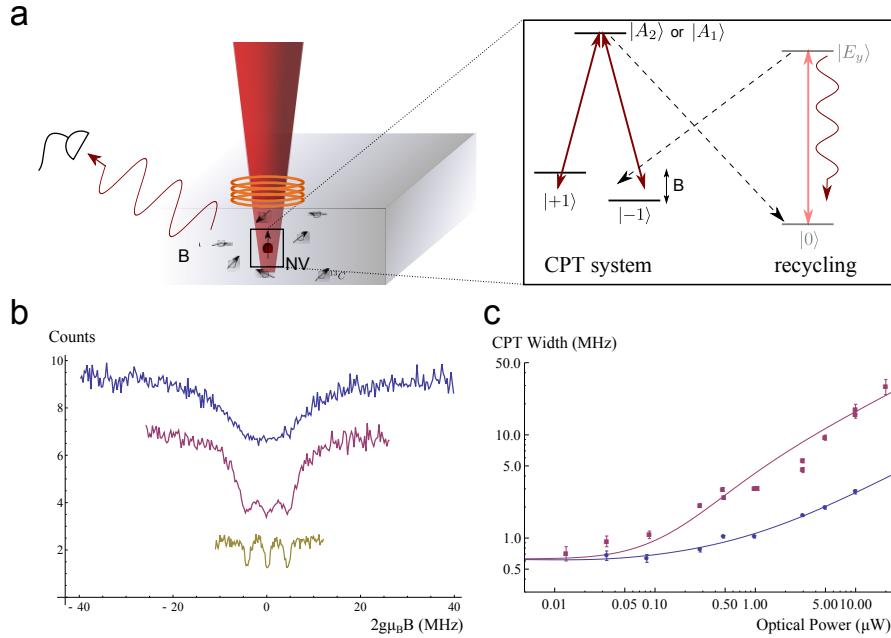
Fig. 1.10 Coherent population trapping in NV centers **a.** The Λ-type transitions between the ground states $|\pm1\rangle$ and excited states $|A_{1,2}\rangle$ of a single NV center are addressed with a CPT laser, while a recycling laser drives the $|0\rangle$ to $|E_y\rangle$ transition. An external magnetic field is applied using a solenoid. **b.** Photon counts from NVa in a 300 μs window are plotted versus the applied field for 10 μW (blue), 3 μW (red), and 0.1 μW (yellow) of laser power addressing the $|A_2\rangle$ state. Blue and red datasets are shifted vertically by 5 and 2 counts for clarity. **c.** Width of individual ^{14}N CPT lines versus CPT laser power when the $|A_1\rangle$ (blue) or $|A_2\rangle$ (red) state is used. Errorbars in all figures show ±1 s.d. Solid curves represent theoretical models. Reprinted from (Togan *et al.*, 2011).

$|A_{1(2)}\rangle$ corresponds to an open (nearly closed) Λ system with $\eta_{A_1} \sim 3.1 \times 10^{-2}$ ($\eta_{A_2} \sim 2.6$). These experimental results are compared with a theoretical model described in (Togan *et al.*, 2011), which predicts that the resonance linewidth δ_0 is given by $\delta_0 = \sqrt{R_A^2 / \left[1 + \frac{1}{\eta}\left(\frac{R_A}{R_E} + \frac{2R_A}{\gamma}\right)\right]} \sim \sqrt{R_A R_E \eta \gamma / (R_E + \gamma)}$ for small η, where $R_{A(E)}$ corresponds to the optical excitation rate by a laser tuned to the $A(E)$ state and γ is the decay rate of excited states. The width at low powers is determined by the random magnetic field associated with surrounding ^{13}C nuclear states. When this line broadening mechanism is taken into account, the experimental results are in excellent agreement with these predictions, plotted as solid lines, showing that a high degree of optical control over the electronic spins of NV center can be achieved.

Subsequent experiments (Togan *et al.*, 2011) showed that CPT can be used for not only probing the nuclear spin environment of the NV center, but also controlling and preparing the state of the spin bath. For the ^{14}N spins, it is possible to optically

cool the nuclear spin states using dark resonances. The physics is reminiscent of laser cooling of atomic motion via velocity-selective CPT (Aspect *et al.*, 1988; Issler *et al.*, 2010). A redistribution of the ^{14}N spin state population upon optical excitation takes place because the hyperfine coupling in the excited electronic state of the NV center is enhanced by a factor of ~ 20 compared to the ground state (Fuchs *et al.*, 2008). If the external field is set such that, for example, the $m_I = 0$ hyperfine states are in two photon resonance, only the states with nuclear configuration $m_I = \pm 1$ will be promoted to the excited states, where flip-flops with the electron spin will change the nuclear spin state to $m_I = 0$. When the NV center spontaneously decays into the dark superposition of electronic spin states, optical excitation will cease, resulting in effective polarization (cooling) of nuclear spin into $m_I = 0$ state.
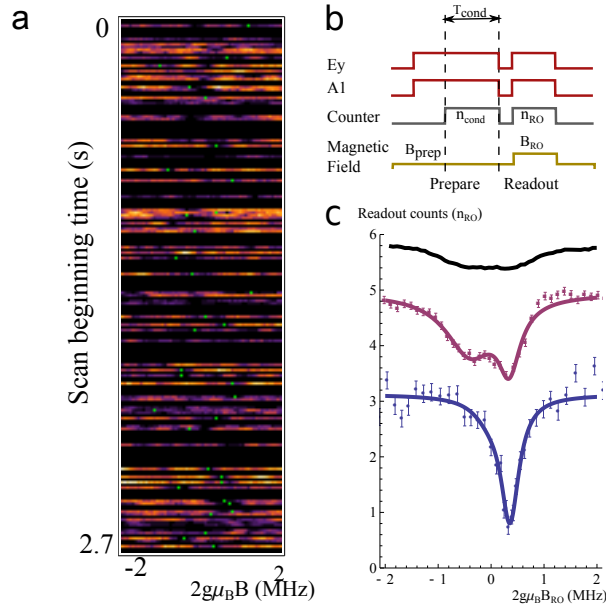
Fig. 1.11 Fast measurement and preparation of ^{13}C spin bath. **a.** Counts from 200 successive fast magnetic field ramps are shown on horizontal lines. The centers of Lorentzian fits to individual runs are indicated with a dot. **b.** Pulse sequence for preparation and subsequent measurement of the ^{13}C configuration. B_{prep} is set within the central ^{14}N line while B_{RO} is varied to cover all associated ^{13}C states. Counts during a conditioning window of length T_{cond} (n_{cond}) at the end of preparation and the readout window (n_{RO}) are recorded for each run. Data presented is an average of many such experimental runs. **b.** n_{RO} versus B_{RO} is shown in the middle plot with double Lorentzian fit. The same dataset analyzed by keeping only events with $n_{\mathrm{cond}} = 0$ is shown in the bottom plot. Unprepared ^{13}C distribution is shown in the top plot for comparison (shifted by 4.3 counts for clarity). Reprinted from (Togan *et al.*, 2011).

We also extended this technique to control the many-body environment of the NV

center, consisting of ^{13}C nuclei distributed throughout the diamond lattice. The large number of nuclear spin configurations associated with an unpolarized environment results in a random Overhasuer field (B_{ov}) with unresolved hyperfine lines. It produces a finite CPT linewidth in measurements that average over all configurations of the ^{13}C spin bath (Figure 1.10b, c). However, one can make use of fast measurements and the long correlation time (T_1^{nuc}) associated with evolution of the nuclear bath to observe its instantaneous state and and manipulate its dynamics. For example, such a fast measurement is illustrated in Figure 1.11a, where the externally applied field is ramped across a single ^{14}N $m_I = 0$ line while the CPT lasers are on, and counts collected in 80 μs time bins are plotted for successive individual runs, many of which distinctly show a narrow dark region. Lorentzian fits to selected experimental scans reveal "instantaneous" CPT resonances with linewidths that are over a factor three less than those of the averaged measurement. The motion of the dark line centers (green dots in Figure 1.11a) indicates that the instantaneous field evolves in time. Fast measurements can also be used to conditionally prepare the ^{13}C environment of the NV center in a desired state with post-selection. Here, the nuclear spins are first prepared though optical excitation at a fixed value of the external magnetic field B_{prep}, as shown in Figure 1.11b. By conditionally selecting zero photon detection events during this preparation step, we can select the states of the ^{13}C environment with vanishing two photon detuning $\delta = 2g\mu_B(B_{\mathrm{prep}} + B_{\mathrm{ov}}) = 0$, where μ_B is the Bohr magneton. The resulting modified distribution of Overhauser field is then probed in a readout step by rapidly the changing magnetic field value to B_{RO}, which is scanned across the resonance. The middle curve in Figure 1.11c shows (unconditioned) readout counts recorded following the preparation step, while the bottom curve shows the result of measurement-based preparation. The measured width of such a conditionally prepared distribution is significantly smaller than the width corresponding to individual ^{14}N resonances obtained without preparation.

1.8   Coherent optical transitions in implanted nitrogen vacancy centers

Since one-of-a-kind natural diamond samples such as the one investigated in the previous sections cannot be used as reproducible starting materials for scalable systems, recent experiments have made use of NV centers incorporated into high quality synthetic diamond during the growth process (Bernien *et al.*, 2012; Acosta *et al.*, 2012; Stacey *et al.*, 2012). In addition to imperfections in their optical coherence, NV centers introduced during the diamond growth process are limited in their usefulness due to their low concentration and random locations. For example, in order to incorporate NV centers into nanophotonic or nanomechanical devices, it is necessary to develop a method to create a controllable concentration of emitters in a well defined device layer while maintaining their excellent optical properties.

This section describes how NV centers can be created in a surface layer that exhibit coherent optical transitions with nearly lifetime-limited linewidths even under the effects of spectral diffusion. We accomplish this by first introducing NV centers at a well defined and controllable depth using ion implantation (Pezzagna *et al.*, 2010). We then demonstrate how to suppress the fundamental cause of spectral diffusion by creating

a diamond environment that is nearly free of defects that contribute to charge fluctuations. This is achieved through a combination of annealing and surface treatments. Finally, we further improve the optical properties of the NV centers by combining our approach with a newly developed technique for preventing photoionization of the remaining charge traps (Siyushev *et al.*, 2013).
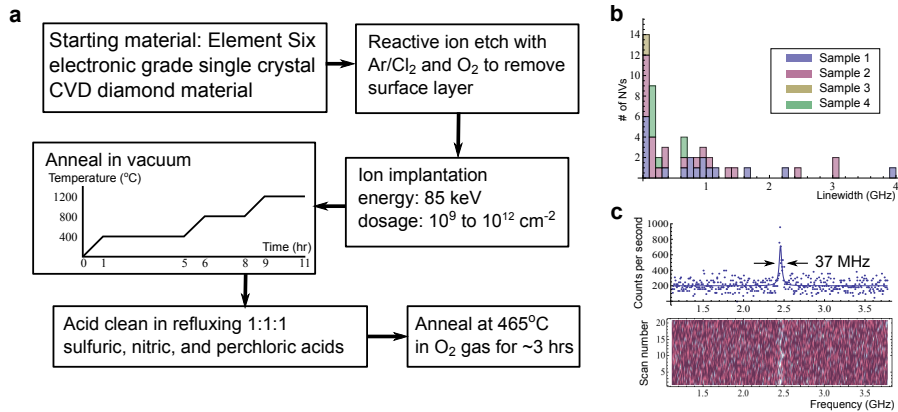
Fig. 1.12 Procedure for creating spectrally stable NV centers through ion implantation, annealing, and surface treatment. The Ar/Cl$_2$ (O$_2$) etch was done using an ICP power of 400 W (700 W), a RF power of 250 W (100 W), a DC bias of 423 V (170 V), a chamber pressure of 8 mTorr (10 mTorr), and a gas flow rate of 25/40 sccm (30 sccm). The sample temperature was set to 17°C. Reprinted from (Chu *et al.* 2014).

Fig. 1.12(a) summarizes the experimental procedure to create shallow implanted NV centers with narrow optical lines. As our starting material we use single crystal diamond from Element Six grown using microwave assisted chemical vapor deposition (CVD). The single crystal samples were homoepitaxial grown on specially prepared ⟨100⟩ oriented synthetic diamond substrates, taking care to ensure that the surface quality of the substrates was as high as possible to reduce sources of dislocations. The CVD synthesis was performed using conditions as described in (Isberg *et al.*, 2002; Markham *et al.*, 2011). The resultant diamond material is measured using electron paramagnetic resonance (EPR) to have a nitrogen concentration of less than 5 parts per billion. The surface layer of these samples is generally damaged and highly strained because of mechanical polishing. Therefore, we first remove the top several micrometers of the sample using a 30 min Ar/Cl$_2$ etch followed by a 20 min O$_2$ etch in an UNAXIS Shuttleline inductively coupled plasma-reactive ion etcher. We then implant ^{15}N$^+$ ions at an energy of 85 keV at a variety of doses from 10^9/cm^2 to 10^{12}/cm^2. According to simulations done using Stopping and Range of Ions in Matter (SRIM), this should result in a mean nitrogen stopping depth of ∼100 nm with a straggle of ∼20 nm (Ziegler, 2013). Subsequently, we anneal the implanted samples under high vacuum ($P < 10^{-6}$ Torr). Our standard annealing recipe consists of a 4 hour 400°C step, a 2 hour 800°C step, and a 2 hour 1200°C step, with a 1 hour ramp up to each

temperature. The motivation behind these temperature steps will be explained later in the text. It is important that a good vacuum is maintained throughout the annealing process, since diamond etches and graphitizes under residual oxidizing gasses at such high temperatures (Seal, 1963). Following the anneal, we remove graphitic carbon and other surface contaminants by cleaning the diamonds for one hour in a 1:1:1 refluxing mixture of sulfuric, nitric, and perchloric acids. Finally, we perform a 465°C anneal in an O_2 atmosphere in a rapid thermal processor (Modular Process Technology, RTP-600xp) in three 48 minute steps following the recipe used in (Fu *et al.*, 2010). This oxygen anneal is believed to remove sp^2 hybridized carbon and result in a more perfect oxygen termination of the surface than acid cleaning alone. We have observed that it enhances charge stability in the NV^- state and helps to reduce blinking and photobleaching.

Let us focus on samples implanted with a $^{15}N^+$ ion dose of $10^{10}/cm^2$. Fig. 1.12(b) shows a histogram of linewidths for 50 NV centers in four such samples. While there is a range of linewidths, a majority of NV centers exhibit linewidths less than 500 MHz, which is comparable to naturally occurring NV centers deep inside electronic grade CVD diamond (Bernien *et al.*, 2012). This is an indication that we have eliminated most impurities with fluctuating charge states in the vicinity of the NV centers, which may include both impurities on the nearby surface and defects inside the diamond introduced by the implantation process. In Fig. 1.12(c), we present an example spectrum of the narrowest linewidth we have observed, along with the results of twenty-one successive PLE scans to demonstrate the long-term stability of the transition line. Our measured linewidth of 37 ± 4.8 MHz under conventional 532 nm repumping is, to the best of our knowledge, a record for the extrinsically broadened linewidth of NV centers.

1.9 Diamond-based nanophotonic devices for quantum optics

1.9.1 Cavity QED with NV centers: the idea

In the previous sections, we have demonstrated the potential of using the NV center's optical properties for a variety of different applications. However, the NV center is not a perfect optical emitter for several reasons. First, the Debye-Waller factor ξ, defined as the ratio of emission into the ZPL vs. the total emission, is only 3-5 %. This is dictated by the relatively large shift in nuclear coordinates between the NV center's ground and excited states, which, by the Franck-Condon principle, results in decay from the excited state into phonon-coupled higher vibrational levels of the ground state (Gali *et al.*, 2011). In addition to such intrinsic properties of the NV center, there are also external effects such as spectral diffusion that result in non-ideal optical properties. While we can eliminate these effects to a large degree, as demonstrated in Chapter 1.8, some residual imperfections in spectral stability usually remain. Additional techniques to stabilize the transition frequency, such as feedback techniques with applied electric fields, reduce the repetition rate of the experiments. Finally, it is generally difficult to extract photons from bulk diamond material with high efficiency. Due to the high index of refraction, total internal reflection confines most of the light inside the diamond at an air interface. In general, as shown in (Plakhotnik *et al.*, 1995), the collection efficiency of a lens or objective with numerical
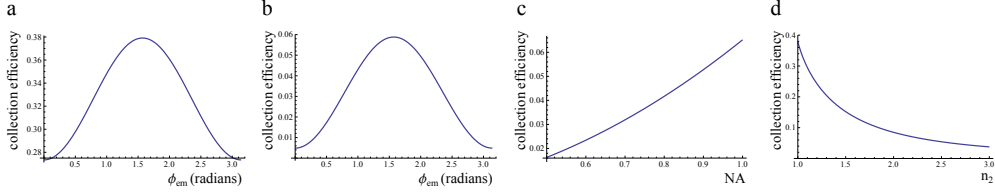
Fig. 1.13 Collection efficiency of light from a dipole emitter. **a.** Collection efficiency vs. dipole orientation for NA=0.95 and n_2=1. **b.** Collection efficiency vs. dipole orientation for NA=0.95 and n_2=2.4. **c.** Collection efficiency vs. NA for $\phi_{em} = \pi/2$ and $n_2 = 2.4$. **d.** Collection efficiency vs. n_2 for $\phi_{em} = \pi/2$ and NA=0.95.

aperture NA in a medium with index n_1 for light from a dipole source in index n_2 is given by

$$C = \frac{1}{8}\left(4 - 3\cos\theta_{max} - \cos^3\theta_{max} + 3(\cos^3\theta_{max} - \cos\theta_{max})\cos^2\phi_{em}\right), \qquad (1.15)$$

where ϕ_{em} is the angle of the dipole axis with the optical axis, and $\theta_{max} = \sin^{-1}(\text{NA} * n_1/n_2)$ is the effective NA of the collection optics. For reference, the collection efficiency is plotted against several parameters in Figure 1.13. As can be seen, even for optimal dipole orientation and a 0.95 NA objective in air, only around 6% of the emitted photons are collected from a NV center in bulk diamond.

The combination of these factors result in a very low rate of indistinguishable, coherent photons from single NV centers. One promising path toward alleviating all of these imperfections is incorporating NV centers with photonic structures. For example, optical cavities can be used to enhance the emission into the ZPL and overcome spectral diffusion, while coupling to waveguide structures can increase the efficiency of photon collection and detection.

The idea of using cavity QED to improve the emission properties of a NV center is as follows: When a NV center is placed inside the an optical cavity, its emission into the cavity mode is enhanced. By tuning the cavity mode to the NV center's ZPL, the ZPL emission is therefore enhanced relative to the PSB emission. When this enhancement becomes larger than the Debye-Waller factor, the ZPL becomes the dominant emission channel of the NV center. This enhancement of the emission also means that the lifetime of the NV center is decreased and the lifetime-limited linewidth of the ZPL is increased. When the lifetime-limited linewidth becomes much larger than the spectral diffusion, the NV center can be viewed as a perfect emitter of indistinguishable photons. In other words, the energy uncertainty of the excited state caused by fast decay into the cavity mode is large enough that the energy uncertainty introduced by spectral jumps is negligible.

We can calculate lifetime of a NV center coupled to the cavity (τ) compared to one that is decoupled from the cavity (τ_0). They are related through a quantity called the Purcell factor, given by

$$P = \frac{3}{4\pi^2}\left(\frac{\lambda_0}{n}\right)^3 \frac{Q}{V}\frac{|\vec{E}_{NV} \cdot \vec{\mu}_{ZPL}|^2}{|\vec{E}_{max}|^2|\vec{\mu}_{NV}|^2} = \frac{\tau_0}{\tau} - 1 \qquad (1.16)$$

where λ_0/n is the wavelength of the resonant mode inside the cavity and Q is the quality factor of the cavity. $\vec{E}_{NV}$ and $\vec{E}_{max}$ are the electric fields at the NV and maximum field inside the cavity, respectively. The mode volume of the cavity is defined as

$$V = \frac{\int |\vec{E}(\vec{x})|^2 dV}{|\vec{E}_{max}|^2} \tag{1.17}$$

Finally, $\vec{\mu}_{ZPL}$ is the effective dipole moment of the ZPL transition, which is the only part coupled to the cavity, while $\vec{\mu}_{NV}$ is the total dipole moment of the NV center. The Debye-Waller factor is then given by $\xi = |\vec{\mu}_{ZPL}|^2/|\vec{\mu}_{NV}|^2$. The Purcell factor gives the enhancement of emission into the cavity mode over the emission when the NV is decoupled from the cavity. Here, we define "decoupled" as an NV that is still spatially located in the cavity, but detuned from the cavity mode in frequency, as is the case in our experiments. This means that n in the expression above is the effective index including all possible modes of the structure. Although this quantity can be difficult to estimate, it is somewhere between 1 and 2.4, the index of bulk diamond.

While the Purcell factor expresses the relevant enhancement of emission in terms of experimentally relevant quantities, it is equivalent to the cooperativity, which gives more physical intuition as simply the ratio between the coupling strength of the emitter to the cavity and the decay rates of the system. The Purcell factor or cooperativity can also be written as

$$P = \frac{2g^2}{\kappa\gamma} \tag{1.18}$$

where $\kappa = \omega/Q$ is the decay rate from the cavity, with ω being the cavity frequency. γ is the decay rate of the NV center into modes other than the resonant cavity mode, and is given by

$$\gamma = \frac{\omega^3 |\mu_{NV}|^2}{3\pi\epsilon\hbar c^3} = \frac{8\pi^2 |\mu_{NV}|^2}{3\epsilon\hbar} \left(\frac{n}{\lambda_0}\right)^3. \tag{1.19}$$

The single-photon Rabi frequency g is given by $g = \vec{E}_{NV} \cdot \vec{\mu}_{ZPL}/\hbar$. We emphasize here that since the cavity mode only couples to the ZPL, we use the effective dipole moment of that transition only. Inserting these expressions into Equation 1.18 and using the fact that $\epsilon \int |\vec{E}(\vec{x})|^2 dV = \hbar\omega$, we recover the expression for the Purcell factor given in Equation 1.16.

We note here that there are several alternative definitions of the Purcell factor that might also relevant here. One can also consider the lifetime change relative to emission into bulk diamond or free space, in which case the index n in Equation 1.16 should be 2.4 or 1, respectively. Another quantity is the enhancement of the ZPL emission into the cavity relative to the ZPL emission when the NV is decoupled from the cavity. This is given by $P' = P/\xi$, and a useful quantity when comparing the Purcell enhancement to other cavity QED systems where the emitter has a single decay channel. In other words, it gives a better comparison for the quality of the emitter-cavity coupling without factoring in the internal imperfections of the emitter itself, and is the quantity usually quoted in the literature. It is also the relevant quantity for estimating the enhancement of the ZPL photon rate from the cavity compared to, say, bulk diamond.

As explained above, in order to radiatively broaden the NV center through Purcell enhancement to overcome spectral diffusion, we require that $P \gg \frac{\Gamma}{\gamma}$, or $P' \gg \frac{1}{\xi}\frac{\Gamma}{\gamma}$, where Γ is the extrinsically broadened linewidth. From Equation 1.16, we see that to obtain a large Purcell factor, we need large Q and small mode volume. This can be achieved using photonic crystal cavities, where the mode volume can be designed to be $\sim (\lambda/n)^3$. Then, for a NV center with $\Gamma \sim 100$ MHz, a cavity with a Q of ~ 3000 is required. We now discuss some directions for the physical implementation of such cavities in diamond.

1.9.2 Diamond-based nanophotonic devices

Over the past several decades, a large range of techniques have been developed for the fabrication of nanoscale devices in semiconductor materials ranging from silicon-based materials to III-V compounds such as gallium arsenide (Englund *et al.*, 2007; Blanco *et al.*, 2000). While many of these techniques can be transferred to the fabrication of diamond, one major difference between diamond and most semiconductor materials presents a significant challenge to the fabrication of nanoscale devices for confining light. Because of the large lattice mismatch of diamond with most other crystalline materials, it is not possible to grow high quality thin films of single crystal diamond on top of a different substrate. This means that we cannot take advantage of the index mismatch between the device and substrate to confine light through total internal reflection. Here, we will briefly describe two methods for creating diamond-based nanophotonic devices by either creating a thin film that is placed on a substrate, or directly fabricating suspended structures on the surface of a bulk diamond sample. The first method for fabricating diamond-based photonic crystal cavities begins with a mechanically polished diamond membrane that is thinned down using a deep reactive ion etch (RIE) in inductively coupled plasma (ICP) of oxygen to the device thickness (Hausmann *et al.*, 2013; Faraon *et al.*, 2011). Devices are then defined on these thin films by e-beam lithography (EBL) using hydrogen silsesquioxane (HSQ) resist, which forms a mask that is transferred into the diamond film during another RIE etching step. The second technique for scalable fabrication of nanophotonic structures involves undercut structures suspended above the surface of bulk diamond. This is achieved using a technique described in (Burek *et al.*, 2012), where the diamond is placed inside a faraday cage during RIE so that the ions are redirected and impinge on the surface at an angle. As a result, instead of etching the diamond in the direction perpendicular to the surface, it undercuts the material beneath the mask from two directions, resulting in suspended structures with a triangular cross-section that are suspended from or supported by anchors. As shown in (Burek *et al.*, 2012) and Figure 1.14, we can make a variety of devices including ring resonators, cantilevers, and 1D photonic crystal cavities using this method. In addition, 1D waveguide structures can be incorporated into hybrid cavities where a Bragg structure is defined by another material around an NV inside the waveguide, such as PMMA.

1.9.3 Example: Purcell enhancement from a coupled NV-cavity system

As an example, we present here a measurement demonstrating the Purcell enhancement of a NV center's ZPL emission by a nanoscale hybrid diamond-PMMA cavity
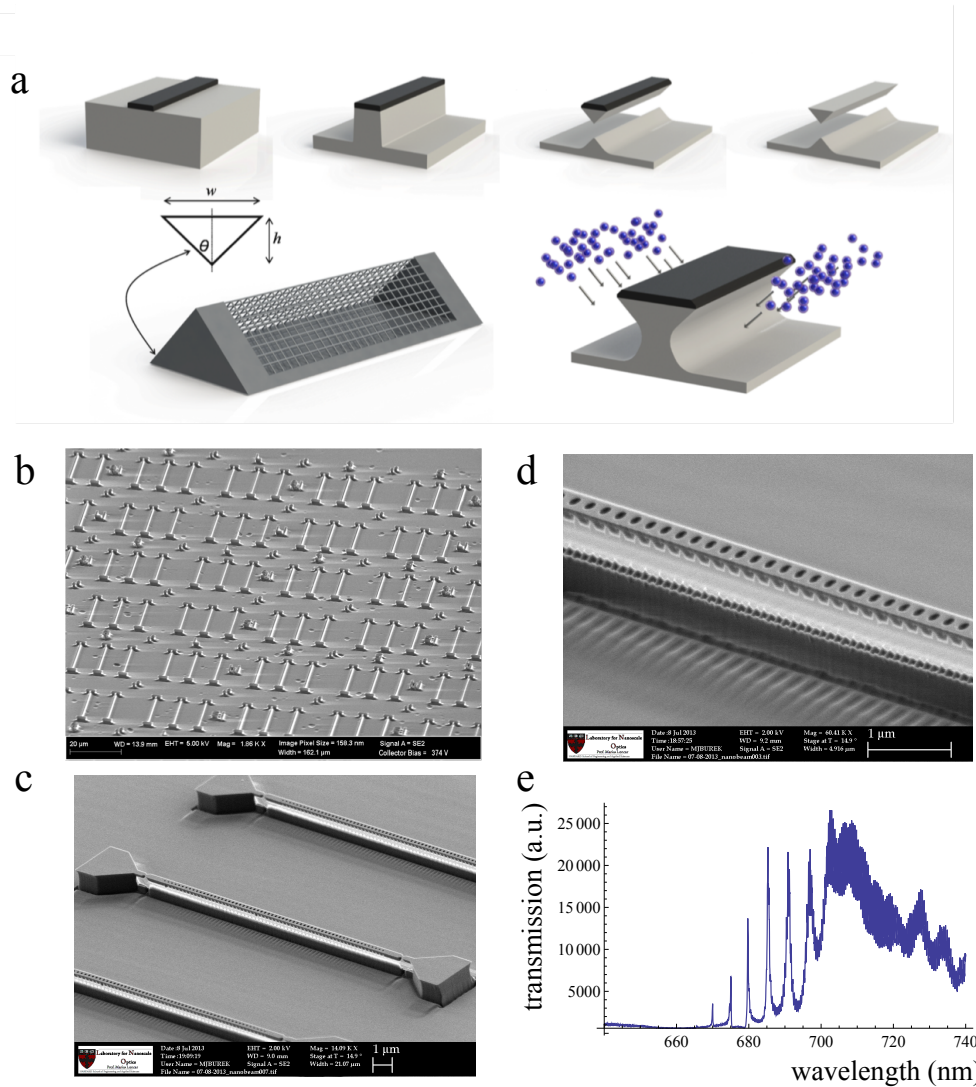
Fig. 1.14 Suspended diamond-based nanophotonic structures. **a.** Procedure for angled RIE etching. A mask is defined using EBL on the surface of the diamond. A top-down etching step performed, followed by an angle-etching step where the diamond is placed in the center of a machined aluminum faraday cage shown on the bottom left. The mask is removed, leaving a suspended structure attached at both ends to anchors (not shown) **b.** SEM image of a large array of ∼1000 angle-etched waveguides. **c-d.** SEM images of photonic crystal cavities formed in 1D waveguides. **e.** Transmission spectrum of one such device. See (Burek *et al.*, 2012) for details.

(de Leon *et al.*, 2014). These measurements were made on a NV center with a 3 GHz linewidth inside a hybrid cavity with a Q of $\sim$600.

In order to tune the cavity mode frequency, we use a combination of two techniques. The first method uses a O_2 plasma etcher (Technics, Model 220) to remove a layer of material from the structure (Hausmann *et al.*, 2013). This tunes the cavity resonance to lower wavelengths because more of the cavity field resides in air than before and therefore has a higher energy. We have been able to achieve a wavelength shift of $\sim$15 nm without significant degradation in the Q factor using this method. Complementary to this blue tuning process, we can also red tune the cavity resonance by depositing neon gas on the structure when it has been cooled down inside the cryostat (Mosor *et al.*, 2005). We note here that gas deposition is a common method for tuning photonic crystal cavities, and a tuning range of $\sim$23 nm was observed in (Hausmann *et al.*, 2013). However, it is somewhat less effective for our hybrid structures since the high aspect ratio of the PMMA slabs prevent the diffusion of gas onto the diamond waveguide, where the field is concentrated. Despite this, we have occasionally been able to obtain tuning ranges of $\sim$6 nm.

To measure the change in lifetime when the NV center becomes coupled with the cavity, we first tune the cavity resonance using plasma etching until it is to the blue of the NV center's ZPL. We then gradually red tune the cavity onto resonance with the ZPL while measuring the lifetime using a filtered supercontinuum laser (NKT photonics, SuperK EXTREME) as a pulsed laser source around 532 nm. As shown in Figure 1.15, the lifetime decreases from 18.5 ns when the cavity is completely off resonant to 11.6 ns when the cavity is tuned to the ZPL. This gives a Purcell factor of $P = 0.59$, or a ZPL enhancement of $P' = 20$ for $\xi = 0.03$. We emphasize here that this enhancement factor implies that the ZPL emission is now $\sim$40% of the total emission from the NV center.

1.10   Outlook

Following the experiments presented in Section 1.6, there has been tremendous progress in using optical photons to connect remote NV centers. Future work will explore the possibility of combining the few-qubit local spin register with the resource of remote entanglement through, for example, teleportation of quantum information between remote, long-lived nuclear spin memories. Distribution of quantum information by teleportation has been demonstrated in several different physical systems (Nölleke *et al.*, 2013; Steffen *et al.*, 2013; Krauter *et al.*, 2013). However, remote teleportation over long distances is an outstanding challenge with solid state systems, which, in the long run, offers the possibility of implementing more scalable local quantum nodes. In particular, one major factor in determining the ultimate bandwidth and fidelity of a remote quantum channel is the efficiency with which single photons can be made to interact with the stationary qubits and then extracted into, for example, a optical fiber. Current photon collection efficiencies and entanglement rates may be sufficient for proof-of-principle experiments, but certainly must be greatly improved for the implementation of practical quantum networks. The work described in Sections 1.8 and 1.9 begins to address this issue. The spectral stability of NV centers is an important factor determining the repetition rate of experiments requiring indistinguishable op-
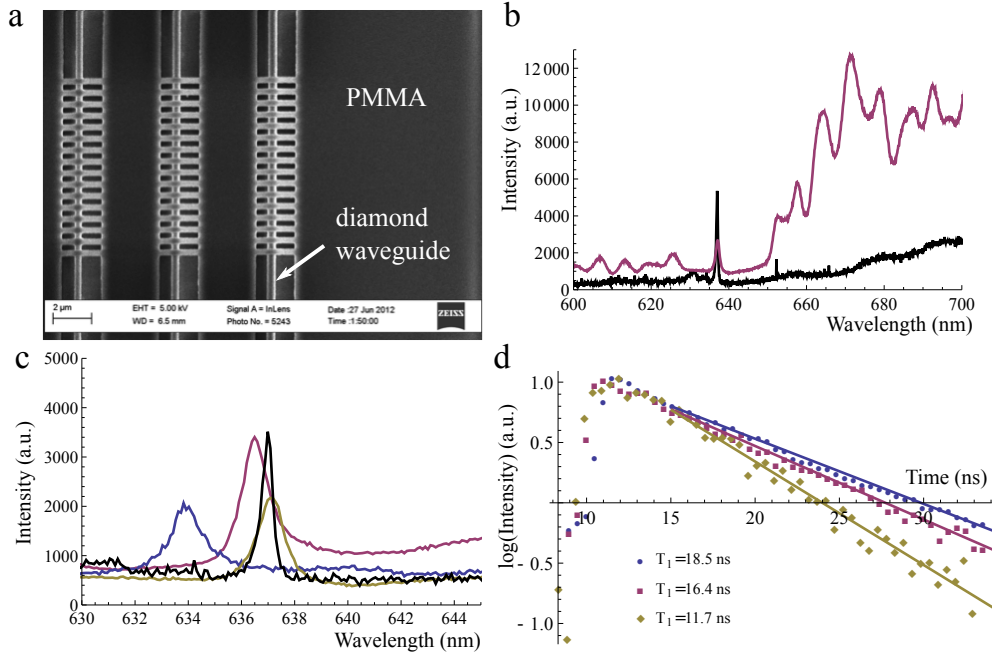
Fig. 1.15 Purcell enhancement of the NV center ZPL emission using hybrid photonic crystal cavities. **a.** SEM image of hybrid diamond-PMMA cavities. Visible are the top surface of the suspended triangular beams, the top of the the PMMA layer and slabs, along with the exposed diamond surface underneath. **b.** Transmission spectrum of hybrid cavity (magenta) and emission spectrum of NV center (black). The spectra have been scaled relative to each other to fit on the same scale. **c.** Zoomed in spectra showing ZPL of NV center (black) and cavity resonance tuned to three different frequencies (blue, magenta, and yellow). **d.** Lifetime measurements corresponding to the detunings in c., taken by exciting the NV center with a pulsed laser and collecting the PSB emission. See (de Leon *et al.*, 2014)

tical photons, such as remote entanglement and teleportation. The availability of NV centers with lifetime-limited linewidths would eliminate the need for active stabilization and post-selection of the the transition frequency in future experiments. Cavity QED has been used to enhance the interaction of photons with atomic systems and improve their collection efficiency, leading to demonstrations of quantum teleportation with high fidelity and success rates (Nölleke *et al.*, 2013). Diamond-based nanophotonics offers the possibility of achieving efficient photonic quantum devices in a solid state system.

Finally, future quantum technologies will most likely be implemented with a combination of several types of physical systems, each with its own strengths and weaknesses. There are already many theoretical proposals and experimental demonstrations of interfacing NV centers with other quantum devices (Kubo *et al.*, 2011; Rabl *et al.*, 2010). Most of these demonstrations make use of the NV center's unique spin properties, effectively turning its interaction with the magnetic environment from a detriment into

a resource. Analogous to this, an potential direction for future exploration would be to take advantage of the NV center's optical transitions to interface it with other systems. Combined with the ability to communicate information with remote systems through optical photons, the NV center becomes a quantum system that not only has uniquely attractive properties as an isolated system, but can also be made to interact with other systems in a controlled manner. Therefore, the ideas and techniques described in this chapter will likely enable researchers to use the optical properties of the NV center as a powerful resource for building complex and useful quantum technologies.

1.11   Acknowledgements

References

Acosta, V. M., Santori, C., Faraon, A., Huang, Z., Fu, K.-M. C., Stacey, A., Simpson, D. A., Ganesan, K., Tomljenovic-Hanic, S., Greentree, A. D., Prawer, S., and Beausoleil, R. G. (2012, May). Dynamic stabilization of the optical resonances of single nitrogen-vacancy centers in diamond. *Phys. Rev. Lett.*, **108**, 206401.

Ansmann, M., Wang, H., Bialczak, R. C., Hofheinz, M., and *et al.*, E. L. (2009). Violation of bell's inequality in josephson phase qubits. *Nature*, **461**, 504–506.

Aslam, N., Waldherr, G., Neumann, P., Jelezko, F., and Wrachtrup, J. (2013). Photo-induced ionization dynamics of the nitrogen vacancy defect in diamond investigated by single-shot charge state detection. *New Journal of Physics*, **15**(1), 013064.

Aspect, A., Arimondo, E., Kaiser, R., Vansteenkiste, N., and Cohen-Tannoudji, C. (1988, Aug). Laser cooling below the one-photon recoil energy by velocity-selective coherent population trapping. *Phys. Rev. Lett.*, **61**(7), 826–829.

Awschalom, D. D., Bassett, L. C., Dzurak, A. S., Hu, E. L., and Petta, J. R. (2013). Quantum spintronics: Engineering and manipulating atom-like spins in semiconductors. *Science*, **339**(6124), 1174–1179.

Balasubramanian, G., Chan, I. Y., Kolesov, R., Al-Hmoud, M., Tisler, J., Shin, C., Kim, C., Wjcik, A., Hemmer, P. R., Krueger, A., Hanke, T., Leitenstorfer, A., Bratschitsch, R., Jelezko, F., and Wrachtrup, J. (2008). Nanoscale imaging magnetometery with diamond spins under ambient conditions. *Nature*, **455**, 648–651.

Balasubramanian, G., Neumann, P., Twitchen, D., Markham, M., Kolesov, R., and *et al.* (2009). Ultralong spin coherence time in isotopically engineered diamond. *Nature Materials*, **8**, 383.

Bassett, L. C., Heremans, F. J., Yale, C. G., Buckley, B. B., and Awschalom, D. D. (2011, Dec). Electrical tuning of single nitrogen-vacancy center optical transitions enhanced by photoinduced fields. *Phys. Rev. Lett.*, **107**, 266403.

Batalov, A., Jacques, V., Kaiser, F., Siyushev, P., Neumann, P., Rogers, L. J., McMurtrie, R. L., Manson, N. B., Jelezko, F., and Wrachtrup, J. (2009, May). Low temperature studies of the excited-state structure of negatively charged nitrogen-vacancy color centers in diamond. *Phys. Rev. Lett.*, **102**(19), 195506.

Batalov, A., Zierl, C., Gaebel, T., Neumann, P., Chan, I.-Y., Balasubramanian, G., Hemmer, P. R., Jelezko, F., and Wrachtrup, J. (2008). Temporal coherence of photons emitted by single nitrogen-vacancy defect centers in diamond using optical rabi-oscillations. *Phys. Rev. Lett.*, **100**, 077401.

Benko, C., Ruehl, A., Martin, M. J., Eikema, K. S. E., Fermann, M. E., Hartl, I., and Ye, J. (2012, Jun). Full phase stabilization of a yb:fiber femtosecond frequency comb via high-bandwidth transducers. *Opt. Lett.*, **37**(12), 2196–2198.

Bernien, H., Childress, L., Robledo, L., Markham, M., Twitchen, D., and Hanson, R. (2012, Jan). Two-photon quantum interference from separate nitrogen vacancy

centers in diamond. *Phys. Rev. Lett.*, **108**, 043604.

Bernien, H., Hensen, B., Pfaff, W., Koolstra, G., Blok, M. S., Robledo, L., Taminiau, T. H., Markham, M., Twitchen, D. J., Childress, L., and Hanson, R. (2013). Heralded entanglement between solid-state qubits separated by three metres. *Nature*, **497**(7447), 86–90.

Blanco, A., Chomski, E., Grabtchak, S., Ibisate, M., John, S., Leonard, S. W., Lopez, C., Meseguer, F., Miguez, H., and Mondia, J. P. (2000). Large-scale synthesis of a silicon photonic crystal with a complete three-dimensional bandgap near 1.5 micrometres. *Nature* (6785), 437–440.

Blinov, B. B., Moehring, D. L., Duan, L. M., and Monroe, C. (2004). Observation of entanglement between a single trapped atom and a single photon. *Nature*, **428**, 153.

Buckley, B. B., Fuchs, G. D., Bassett, L. C., and Awschalom, D. D. (2010). Spin-light coherence for single-spin measurement and control in diamond. *Science*, **330**(6008), 1212–1215.

Budker, D. and Romalis, M. (2007). Optical magnetometry. *Nature Physics*, **3**, 227–234.

Burek, M. J., de Leon, N. P., Shields, B. J., Hausmann, B. J. M., Chu, Y., Quan, Q., Zibrov, A. S., Park, H., Lukin, M. D., and Loncar, M. (2012). Free-standing mechanical and photonic nanostructures in single-crystal diamond. *Nano Letters*, **12**(12), 6084–6089.

Childress, L., Gurudev Dutt, M. V., Taylor, J. M., Zibrov, A. S., Jelezko, F., Wrachtrup, J., Hemmer, P. R., and Lukin, M. D. (2006). Coherent dynamics of coupled electron and nuclear spin qubits in diamond. *Science*, **314**(5797), 281–285.

Chou, C. W., Hume, D. B., Koelemeij, J. C. J., Wineland, D. J., and Rosenband, T. (2010, Feb). Frequency comparison of two high-accuracy al$^+$ optical clocks. *Phys. Rev. Lett.*, **104**, 070802.

Clarke, J. and Wilhelm, F. K. (2008). Superconducting quantum bits. *Nature*, **453**(7198), 1031–1042.

de Leon, N. P., Burek, M. J., Chu, Y., de Greve, K., Evans, R., Hausmann, B. J. M., High, A., Maletinsky, P., Markham, M., Polking, M., Shields, B. J., Stacey, A., Togan, E., Twitchen, D. J., Zibrov, A. S., Yacoby, A., Park, H., Loncar, M., and Lukin, M. D. (2014). In preparation.

de Riedmatten, H., Afzelius, M., Staudt, M. U., Simon, C., and Gisin, N. (2008). A solid-state light-matter interface at the single-photon level. *Nature*, **456**, 773.

DiCarlo, L., Chow, J. M., Bishop, J. M. G. L. S., Johnson, B. R., and *et al.* (2009). Demonstration of two-qubit algorithms with a superconducting quantum processor. *Nature*, **46**, 240–244.

Doherty, M. W., Dolde, F., Fedder, H., Jelezko, F., Wrachtrup, J., Manson, N. B., and Hollenberg, L. C. L. (2012, May). Theory of the ground-state spin of the nv center in diamond. *Phys. Rev. B*, **85**, 205203.

Doherty, M. W., Manson, N. B., Delaney, P., and Hollenberg, L. C. (2010). The negatively charged nitrogen-vacancy centre in diamond: the electronic solution. *arXiv:1008.5224*.

Doherty, M. W., Manson, N. B., Delaney, P., Jelezko, F., Wrachtrup, J., and Hol-

lenberg, L. C. (2013). The nitrogen-vacancy colour centre in diamond. *Physics Reports*, **528**(1), 1 – 45.

Duan, L.-M. and Monroe, C. (2008). Robust quantum information processing with atoms, photons, and atomic ensembles. *Advances in Atomic, Molecular, and Optical Physics*, **55**, 419–464.

Dutt, M. V. G., Childress, L., Jiang, L., Togan, E., Maze, J., and *et al.* (2007). Quantum register based on individual electronic and nuclear spin qubits in diamond. *Science*, **316**, 1312.

Englund, D., Faraon, A., Fushman, I., Stoltz, N., Petroff, P., and Vuckovic;, J. (2007). Controlling cavity reflectivity with a single quantum dot. *Nature* (7171), 857–861.

Faraon, A., Barclay, P., Santori, C., Fu, K., and Beausoleil, R. (2011). Resonant enhancement of the zero-phonon emission from a colour centre in a diamond cavity. *Nature Photon.*, **5**(5), 301–305.

Fleischhauer, M., Imamoglu, A., and Marangos, J. P. (2005). Electromagnetically induced transparency: Optics in coherent media. *Rev. Mod. Phys.*, **77**, 633.

Fu, K.-M. C., Santori, C., Barclay, P. E., and Beausoleil, R. G. (2010). Conversion of neutral nitrogen-vacancy centers to negatively charged nitrogen-vacancy centers through selective oxidation. *Applied Physics Letters*, **96**(12), 121907.

Fu, K.-M. C., Santori, C., Barclay, P. E., Rogers, L. J., Manson, N. B., and Beausoleil, R. G. (2009, Dec). Observation of the dynamic jahn-teller effect in the excited states of nitrogen-vacancy centers in diamond. *Phys. Rev. Lett.*, **103**, 256404.

Fuchs, G. D., Dobrovitski, V. V., Hanson, R., Batra, A., Weis, C. D., Schenkel, T., and Awschalom, D. D. (2008, Sep). Excited-state spectroscopy using single spin manipulation in diamond. *Phys. Rev. Lett.*, **101**(11), 117601.

Fuchs, G. D., Dobrovitski, V. V., Toyli, D. M., Heremans, F. J., and Awschalom, D. D. (2009). Gigahertz dynamics of a strongly driven single quantum spin. *Science*, **326**, 1520.

Gali, A., Fyta, M., and Kaxiras, E. (2008). Ab initio supercell calculations on nitrogen-vacancy center in diamond: Electronic structure and hyperfine tensors. *Phys. Rev. B*, **77**, 155206.

Gali, A., Simon, T., and Lowther, J. E. (2011). An ab initio study of local vibration modes of the nitrogen-vacancy center in diamond. *New Journal of Physics*, **13**(2), 025016.

Giedke, G., Taylor, J. M., D'Alessandro, D., Lukin, M. D., and Imamoglu, A. (2006, Sep). Quantum measurement of a mesoscopic spin ensemble. *Phys. Rev. A*, **74**(3), 032316.

Goss, J., Jones, R., Breuer, S., Briddon, P., and Oberg, S. (1996). The twelve-line 1.682 ev luminescence center in diamond and the vacancy-silicon complex. *Phys. Rev. Lett.*, **77**, 3041.

Gruber, A., Drbenstedt, A., Tietz, C., Fleury, L., Wrachtrup, J., and Borczyskowski, C. v. (1997). Scanning confocal optical microscopy and magnetic resonance on single defect centers. *Science*, **276**(5321), 2012–2014.

Hausmann, B. J. M., Shields, B. J., Quan, Q., Chu, Y., de Leon, N. P., Evans, R., Burek, M. J., Zibrov, A. S., Markham, M., Twitchen, D. J., Park, H., Lukin, M. D., and Loncr, M. (2013). Coupling of nv centers to photonic crystal nanobeams in

diamond. *Nano Letters*, **13**(12), 5791–5796.

Isberg, J., Hammersberg, J., Johansson, E., Wikstrm, T., Twitchen, D. J., Whitehead, A. J., Coe, S. E., and Scarsbrook, G. A. (2002). High carrier mobility in single-crystal plasma-deposited diamond. *Science*, **297**(5587), 1670–1672.

Issler, M., Kessler, E. M., Giedke, G., Yelin, S., Cirac, I., Lukin, M. D., and Imamoglu, A. (2010, Dec). Nuclear spin cooling using overhauser-field selective coherent population trapping. *Phys. Rev. Lett.*, **105**(26), 267202.

Jelezko, F. and Wrachtrup, J. (2006). Quantum information processing in diamond. *J. Phys.: Condens. Matter*, **18**, S807–824.

Kaiser, F., Jacques, V., Batalov, A., Siyushev, P., Jelezko, F., and Wrachtrup, J. (2009). Polarization properties of single photons emitted by nitrogen-vacancy defect in diamond at low temperature. *arXiv:0906.3426*.

Kessler, T., Hagemann, C., Grebing, C., Legero, T., Sterr, U., Riehle, F., Martin, M. J., Chen, L., and Ye, J. (2012). A sub-40-mhz-linewidth laser based on a silicon single-crystal optical cavity. *Nature Photonics* (10), 687–692.

Kimble, H. J. (2008). The quantum internet. *Nature*, **453**, 1023.

Krauter, H., Salart, D., Muschik, C. A., Petersen, J. M., Shen, H., Fernholz, T., and Polzik, E. S. (2013). Deterministic quantum teleportation between distant atomic objects. *Nature Physics* (7), 400–404.

Kubo, Y., Grezes, C., Dewes, A., Umeda, T., Isoya, J., Sumiya, H., Morishita, N., Abe, H., Onoda, S., Ohshima, T., Jacques, V., Dréau, A., Roch, J.-F., Diniz, I., Auffeves, A., Vion, D., Esteve, D., and Bertet, P. (2011, Nov). Hybrid quantum circuit with a superconducting qubit coupled to a spin ensemble. *Phys. Rev. Lett.*, **107**, 220501.

Kurtsiefer, C., Mayer, S., Zarda, P., and Weinfurter, H. (2000, July). Stable solid-state source of single photons. *Phys. Rev. Lett.*, **85**(2), 290–293.

Lenef, A. and Rand, S. (1996). Electronic structure of the nv center in diamond: Theory. *Phys. Rev. B*, **53**, 13441.

Lloyd, S. (1996). Universal quantum simulators. *Science*, **273**(5278), 1073–1078.

Loubser, J. and Wyk, J. V. (1978). Electron spin resonance in the study of diamond. *Rep. Prog. Phys.*, **91**, 1201.

Manson, N. B., Harrison, J. P., and Sellars, M. J. (2006, Sep). Nitrogen-vacancy center in diamond: Model of the electronic structure and associated dynamics. *Phys. Rev. B*, **74**, 104303.

Markham, M., Dodson, J., Scarsbrook, G., Twitchen, D., Balasubramanian, G., Jelezko, F., and Wrachtrup, J. (2011). {CVD} diamond for spintronics. *Diamond and Related Materials*, **20**(2), 134 – 139.

Maze, J., Gali, A., Togan, E., Chu, Y., Trifonov, A., Kaxiras, E., and Lukin, M. (2011). Properties of nitrogen-vacancy centers in diamond: the group theoretic approach. *New J. Phys.*, **13**, 025025.

Maze, J., Stanwix, P. L., Hodges, J. S., Hong, S., Taylor, J. M., Cappellaro, P., Jiang, L., Dutt, M. V. G., Togan, E., Zibrov, A. S., Yacoby, A., Walsworth, R. L., and Lukin, M. D. (2008). Nanoscale magnetic sensing with an individual electronic spin in diamond. *Nature*, **455**, 644–647.

Monroe, C. and Kim, J. (2013). Scaling the ion trap quantum processor. *Science*, **339**(6124), 1164–1169.

Mosor, S., Hendrickson, J., Richards, B. C., Sweet, J., Khitrova, G., Gibbs, H. M., Yoshie, T., Scherer, A., Shchekin, O. B., and Deppe, D. G. (2005). Scanning a photonic crystal slab nanocavity by condensation of xenon. *Applied Physics Letters*, **87**(14), 141105.

Neumann, P., Beck, J., Steiner, M., Rempp, F., Fedder, H., Hemmer, P. R., Wrachtrup, J., and Jelezko, F. (2010). Single-shot readout of a single nuclear spin. *Science*, **329**, 542.

Neumann, P., Mizuochi, N., Rempp, F., Hemmer, P., Watanabe, H., Yamasaki, S., Jacques, V., Gaebel, T., Jelezko, F., and Wrachtrup, J. (2008). Multipartate entanglement among single spins in diamond. *Science*, **320**, 1326–1329.

Ni, K.-K., Ospelkaus, S., de Miranda, M. H. G., Pe'er, A., Neyenhuis, B., Zirbel, J. J., Kotochigova, S., Julienne, P. S., Jin, D. S., and Ye, J. (2008). A high phase-space-density gas of polar molecules. *Science*, **322**(5899), 231–235.

Nicholson, T. L., Martin, M. J., Williams, J. R., Bloom, B. J., Bishof, M., Swallows, M. D., Campbell, S. L., and Ye, J. (2012, Dec). Comparison of two independent sr optical clocks with 1×10^{-17} stability at 10^3 s. *Phys. Rev. Lett.*, **109**, 230801.

Nölleke, C., Neuzner, A., Reiserer, A., Hahn, C., Rempe, G., and Ritter, S. (2013, Apr). Efficient teleportation between remote single-atom quantum memories. *Phys. Rev. Lett.*, **110**, 140403.

Pezzagna, S., Naydenov, B., Jelezko, F., Wrachtrup, J., and Meijer, J. (2010). Creation efficiency of nitrogen-vacancy centres in diamond. *New Journal of Physics*, **12**(6), 065017.

Plakhotnik, T., Moerner, W., Palm, V., and Wild, U. P. (1995). Single molecule spectroscopy: maximum emission rate and saturation intensity. *Optics Communications*, **114**(1-2), 83 – 88.

Platzman, P. M. and Dykman, M. I. (1999). Quantum computing with electrons floating on liquid helium. *Science*, **284**(5422), 1967–1969.

Rabl, P., Kolkowitz, S. J., Koppens, F. H. L., Harris, J. G. E., Zoller, P., and Lukin, M. D. (2010). A quantum spin transducer based on nanoelectromechanical resonator arrays. *Nature Physics* (8), 602–608.

Robledo, L., Bernien, H., van Weperen, I., and Hanson, R. (2010, Oct). Control and coherence of the optical transition of single nitrogen vacancy centers in diamond. *Phys. Rev. Lett.*, **105**, 177403.

Robledo, L., Childress, L., Bernien, H., Hensen, B., Alkemade, P. F. A., and Hanson, R. (2011). High-fidelity projective read-out of a solid-state spin quantum register. *Nature*, **477**, 574–578.

Rogers, L., McMurtrie, R., Sellars, M., and Manson, N. B. (2009). Time-averaging within the excited state of the nitrogen-vacancy centre in diamond. *New Journal of Physics*, **11**, 063007.

Santori, C., Tamarat, P., Neumann, P., Wrachtrup, J., Fattal, D., Beausoleil, R. G., Rabeau, J., Olivero, P., Greentree, A. D., Prawer, S., Jelezko, F., and Hemmer, P. (2006, Dec). Coherent population trapping of single spins in diamond under optical excitation. *Phys. Rev. Lett.*, **97**(24), 247401.

Scully, M. O. and Druhl, K. (1982). Quantum eraser: A proposed photon correlation experiment concerning observation and "delayed choice" in quantum mechanics.

Phys. Rev. A., **25**, 2208.

Scully, M. O. and Fleischhauer, M. (1992, Aug). High-sensitivity magnetometer based on index-enhanced media. *Phys. Rev. Lett.*, **69**(9), 1360–1363.

Scully, M. O. and Zubairy, M. S. (1997). *Quantum Optics*. Cambridge University Press.

Seal, M. (1963). The effect of surface orientation on the graphitization of diamond. *Physica Status Solidi (b)*, **3**(4), 658–664.

Shen, Y., Sweeney, T. M., and Wang, H. (2008, Jan). Zero-phonon linewidth of single nitrogen vacancy centers in diamond nanocrystals. *Phys. Rev. B*, **77**, 033201.

Shor, P. (1994). Algorithms for quantum computation: discrete logarithms and factoring. In *Foundations of Computer Science, 1994 Proceedings., 35th Annual Symposium on*, pp. 124–134.

Sipahigil, A., Goldman, M. L., Togan, E., Chu, Y., Markham, M., Twitchen, D. J., Zibrov, A. S., Kubanek, A., and Lukin, M. D. (2012, Apr). Quantum interference of single photons from remote nitrogen-vacancy centers in diamond. *Phys. Rev. Lett.*, **108**, 143601.

Siyushev, P., Pinto, H., Vörös, M., Gali, A., Jelezko, F., and Wrachtrup, J. (2013, Apr). Optically controlled switching of the charge state of a single nitrogen-vacancy center in diamond at cryogenic temperatures. *Phys. Rev. Lett.*, **110**, 167402.

Stacey, A., Simpson, D. A., Karle, T. J., Gibson, B. C., Acosta, V. M., Huang, Z., Fu, K. M. C., Santori, C., Beausoleil, R. G., McGuinness, L. P., Ganesan, K., Tomljenovic-Hanic, S., Greentree, A. D., and Prawer, S. (2012). Near-surface spectrally stable nitrogen vacancy centres engineered in single crystal diamond. *Advanced Materials*, **24**(25), 3333–3338.

Steffen, L., Salathe, Y., Oppliger, M., Kurpiers, P., Baur, M., Lang, C., Eichler, C., Puebla-Hellmann, G., Fedorov, A., and Wallraff, A. (2013). Deterministic quantum teleportation with feed-forward in a solid state system. *Nature* (7462), 319–322.

Stepanenko, D., Burkard, G., Giedke, G., and Imamoglu, A. (2006, Apr). Enhancement of electron spin coherence by optical preparation of nuclear spins. *Phys. Rev. Lett.*, **96**(13), 136401.

Stern, A. and Lindner, N. H. (2013). Topological quantum computationfrom basic concepts to first experiments. *Science*, **339**(6124), 1179–1184.

Tamarat, P., Gaebel, T., Rabeau, J. R., Khan, M., Greentree, A. D., Wilson, H., Hollenberg, L. C. L., Prawer, S., Hemmer, P., Jelezko, F., and Wrachtrup, J. (2006, Aug). Stark shift control of single optical centers in diamond. *Phys. Rev. Lett.*, **97**, 083002.

Tamarat, P., Manson, N. B., Harrison, J. P., McMurtie, R. K., Nizovtsev, A., and *et al.* (2008). Spin-flip and spin-conserving optical transitions of the nitrogen-vacancy centre in diamond. *New J. Phys*, **10**, 045004.

Togan, E., Chu, Y., Imamoglu, A., and Lukin, M. D. (2011). Laser cooling and real-time measurement of the nuclear spin environment of a solid-state qubit. *Nature*, **478**(7370), 497–501.

Togan, E., Chu, Y., Trifonov, A. S., Jiang, L., Maze, J., Childress, L., Dutt, M. V. G., Sørensen, A. S., Hemmer, P. R., Zibrov, A. S., and Lukin, M. D. (2010, August). Quantum entanglement between an optical photon and a solid-state spin qubit.

Nature (London), **466**(7307), 730–734.

Vanier, J. (2005). Atomic clocks based on coherent population trapping: a review. *Applied Physics B: Lasers and Optics*, **81**, 421–442.

Wilk, T., Webster, S. C., and A. Kuhn, G. R. (2007). Single-atom single-photon quantum interface. *Science*, **317**, 488–490.

Zaitsev, A. M. (2010). *Optical Properties of Diamond: A Data Handbook*. Springer.

Ziegler, J. F. (2013). Particle interactions with matter. http://www.srim.org.